Cell

Uncovering spatially resolved functional genomics with CRISPR screen sequencing

Graphical abstract

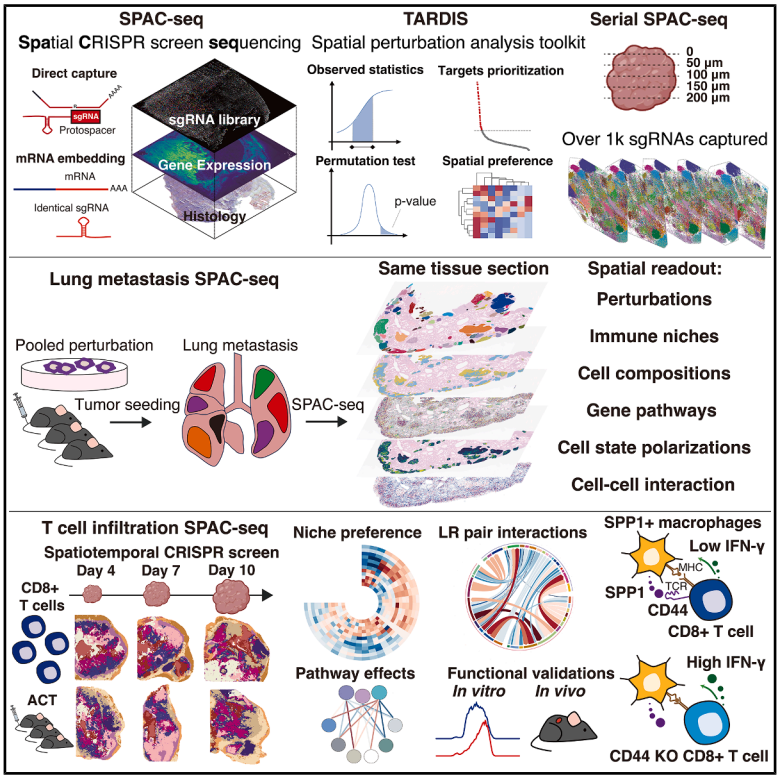

Highlights

- SPAC-seq captures spatially resolved sgRNAs alongside whole-transcriptome profiles
- TARDIS enables target prioritization from spatially resolved phenotypic readouts
- *Icam1* loss promotes tumor metastasis via a spatially defined immunosuppressive niche
- Spatiotemporal screens reveal the SPP1-CD44 macrophage-T cell axis

Authors

Haorui Zhang, Zongxu Zhang, Peiyu Wang, ..., Yu Feng, Deng Pan, Zexian Zeng

Correspondence

fengyu1@genomics.cn (Y.F.), dpan@tsinghua.edu.cn (D.P.), zexianzeng@pku.edu.cn (Z.Z.)

In brief

Zhang et al. present SPAC-seq, a sequencing-based spatial CRISPR screening technology capturing high-throughput perturbation libraries and spatial whole transcriptomes. Complementing this, TARDIS is developed as a statistical toolkit for spatial perturbation analysis. Together, they facilitate discoveries in spatial functional genomics, including cell localization, microenvironmental organization, pathway regulation, and ligand-receptor interactions.

Zhang et al., 2026, Cell *189*, 1–25
July 23, 2026
https://doi.org/10.1016/j.cell.2026.04.049

Please cite this article in press as: Zhang et al., Uncovering spatially resolved functional genomics with CRISPR screen sequencing, Cell (2026), https://doi.org/10.1016/j.cell.2026.04.049

Cell

CellPress
OPEN ACCESS

Article

Uncovering spatially resolved functional genomics with CRISPR screen sequencing

Haorui Zhang,[1,14] Zongxu Zhang,[2,14] Peiyu Wang,[1,2,14] Tian Xu,[1,2] Xiaoyu Chen,[3] Yanping Zhao,[4] Siyu Lin,[1] Wenjie Cai,[1] Pengfei Ren,[1,2] Ce Luo,[1] Peng Zhang,[1] Yunfeng Wang,[1,2] Sen Hou,[5] Yahui Zhao,[6] Hu Zeng,[1] Zhihua Liu,[6] Cunyu Wang,[7] Zhidong Gao,[5] Yu Feng,[8,9,*] Deng Pan,[10,11,*] and Zexian Zeng[1,2,12,13,15,16,*]

[1]Peking-Tsinghua Center for Life Sciences, Academy for Advanced Interdisciplinary Studies, Peking University, Beijing 100084, China
[2]Center for Quantitative Biology, Academy for Advanced Interdisciplinary Studies, Peking University, Beijing 100084, China
[3]BGI Research, Hangzhou 310030, China
[4]Tsinghua-Peking Center for Life Sciences, School of Life Sciences, Tsinghua University, Beijing 100084, China
[5]Department of Gastroenterological Surgery, Peking University People's Hospital, Beijing 100084, China
[6]State Key Laboratory of Molecular Oncology, National Cancer Center, National Clinical Research Center for Cancer, Cancer Hospital, Chinese Academy of Medical Sciences, and Peking Union Medical College, Beijing 100021, China
[7]Beijing Advanced Center of Cellular Homeostasis and Aging-Related Diseases, Institute of Advanced Clinical Medicine, Peking University, Beijing 100871, China
[8]State Key Laboratory of Genome and Multi-omics Technologies, BGI Research, Shenzhen 518083, China
[9]BGI Collaborative Center for Future Medicine, Shanxi Medical University, Taiyuan 030001, China
[10]School of Basic Medical Sciences, Tsinghua University, Beijing 100084, China
[11]Tsinghua-Peking Center for Life Sciences, Tsinghua University, Beijing 100084, China
[12]Peking University Chengdu Academy for Advanced Interdisciplinary Biotechnologies, Chengdu 610213, Sichuan, China
[13]Present address: No.5 Yiheyuan Road, Haidian District, Beijing 100871, P.R. China
[14]These authors contributed equally
[15]Senior author
[16]Lead contact
*Correspondence: fengyu1@genomics.cn (Y.F.), dpan@tsinghua.edu.cn (D.P.), zexianzeng@pku.edu.cn (Z.Z.)
https://doi.org/10.1016/j.cell.2026.04.049

SUMMARY

Spatial omics has advanced our understanding of tissue-level biology, yet tools to systematically link gene functional perturbations to spatial phenotypes and signaling pathways remain limited. To address this, we developed spatial CRISPR screen sequencing (SPAC-seq), a high-throughput spatial CRISPR screen platform, and TARDIS (target prioritization toolkit for perturbation data in spatial omics), a statistical spatial perturbation analysis toolkit. Using SPAC-seq and TARDIS, we linked gene perturbations to spatial phenotypes and pathways, uncovering how *Icam1* loss in tumor cells promotes metastasis via immune suppression and macrophage polarization. In $CD8^+$ T cells, we revealed *Cd44*'s role in regulating spatial phenotypes by interacting with *Spp1* on macrophages. We also demonstrated the model of the transcription factor-chemokine receptor axis coupling cell states with chemotaxis. SPAC-seq and TARDIS provide an effective framework to study spatially resolved functional genomics and pathways across diverse biological and disease contexts.

INTRODUCTION

Biological systems are inherently spatially organized, with cellular interactions and molecular processes occurring within specific spatial contexts.[1] Among the advanced tools in the field of spatial biology, spatial transcriptomics has been proven to be a powerful methodology, enabling the study of tissue structure, spatially embedded gene-expression patterns, cellular communities, and cellular interactions.[2–4] The recent advent of spatial transcriptomics, which now enables transcriptome-wide profiling at single-cell resolution, has provided unprecedented opportunities to investigate complex tissue ecosystems, such as the tumor microenvironment (TME).[5] However, tools to establish causal links between gene expression and its functional effects on spatial phenotypes, as well as the regulatory pathways driving these processes, remain largely underdeveloped.

CRISPR-Cas9-based gene editing, which uses sgRNAs to direct the Cas9 protein for targeted genome editing, has revolutionized functional genomics by directly linking gene perturbations to specific phenotypes, such as cell growth, viability, and marker gene expression.[6–8] This approach can be scaled to high-throughput levels using pooled CRISPR screens, enabling systematic investigation of gene functions.[9–11] The advent of single-cell RNA sequencing (scRNA-seq) has further extended

Please cite this article in press as: Zhang et al., Uncovering spatially resolved functional genomics with CRISPR screen sequencing, Cell (2026), https://doi.org/10.1016/j.cell.2026.04.049

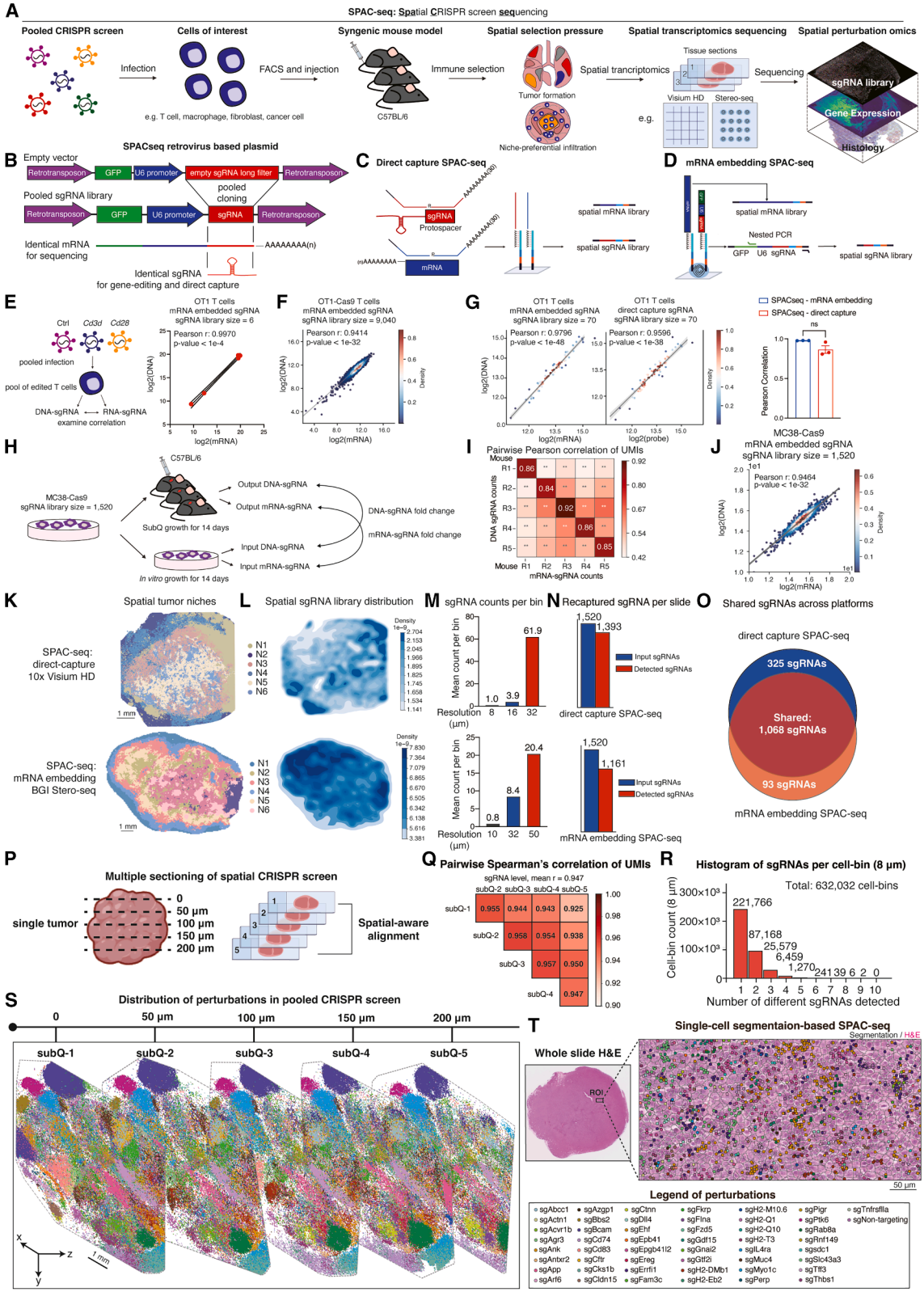

(legend on next page)

Please cite this article in press as: Zhang et al., Uncovering spatially resolved functional genomics with CRISPR screen sequencing, Cell (2026), https://doi.org/10.1016/j.cell.2026.04.049

these capabilities by enabling transcriptome-wide gene-expression profiling in perturbed single cells, exemplified by platforms such as Perturb-seq and CROP-seq.[12–15] Incorporating pooled CRISPR screens with spatial transcriptomics offers a unique opportunity to identify genes associated with spatial functional phenotypes and elucidate the underlying regulatory pathways. Efforts have utilized spatial proteomic imaging to characterize immune-infiltration phenotypes based on marker proteins within specific locally expanded perturbations.[16,17] More recently, spatially resolved detection of sgRNA libraries has been explored using imaging-based methods,[18–22] paving the way for future spatially resolved CRISPR screens that integrate sgRNA and transcriptome detection.[23,24] Sequencing-based spatial CRISPR screens offer a high-throughput approach to connect gene function and regulatory pathways to spatial phenotypes, addressing the gap for transcriptome-wide analysis in spatial biology. In this study, we developed spatial CRISPR screen sequencing (SPAC-seq), coupled with a statistical spatial perturbation analysis toolkit, TARDIS, to leverage the single-cell-resolution spatial whole transcriptome to enable spatially resolved functional genomics.

RESULTS

SPAC-seq for spatial CRISPR screen and spatial transcriptomics sequencing

The SPAC-seq workflow begins with transducing a pooled sgRNA (single guide RNA) library into cell types of interest. After fluorescence-based sorting, the perturbed cells are injected into syngeneic mouse models at specific sites or organs. Following *in vivo* biological selection processes such as tumor metastasis or T cell infiltration, target tissues are harvested, sectioned into slides, and analyzed using single-cell-resolution spatial transcriptomics platforms such as Visium HD or Stereo-seq.[25,26] Both sgRNA library and mRNA are captured *in situ*, enabling next-generation sequencing (NGS) to map sgRNA and transcriptome data to their spatial locations (Figure 1A). SPAC-seq utilizes a retrovirus-based plasmid system, named SPACseq, which incorporates two retrotransposon cassettes: a strong universal promoter and a transcription terminator (Figure 1B),[27,28] designed to ensure efficient transduction and expression in mouse primary cells.[29–31] SPACseq plasmid includes a GFP fluorescence marker for cell sorting and a U6 promoter for sgRNA transcription via RNA polymerase III (RNA Pol III). The sgRNA cassette was designed for high-throughput pooled-library cloning and was embedded within the mRNA encoding GFP, transcribed by the retroviral promoter via RNA polymerase II (RNA Pol II) (Figure 1B). This embedding approach, instead of using an extra barcoding library,[12] eliminates the additional barcoding association steps and reduces recombination risk for sgRNA and barcode regions.[32]

We applied SPAC-seq to two single-cell-resolution spatial transcriptome sequencing platforms, Visium HD and Stereo-seq[25,26] (Figures 1C and 1D). For 10× Visium HD,[25] which uses RNA-specific probes to capture mRNA *in situ*,[25] we designed direct-capture probes specific to the sgRNA spacer sequence and scaffold region, enabling direct capture of the sgRNA sequence *in situ* (Figure 1C). Notably, direct sgRNA capture can be compatible with standard CRISPR vectors. For Stereo-seq, which uses poly(dT) probes on DNA-nanoball chips,[26] we captured mRNA-embedded sgRNAs alongside other transcripts (Figure 1D). This approach is analogous to sgRNA detection in CROP-seq.[13] Together, SPAC-seq is scalable across different plasmids and spatial transcriptome platforms.

We conducted a series of evaluation assays to assess transduction efficiency, gene-editing efficiency, sgRNA detection signals, and detection accuracy of SPACseq plasmid. First, we assessed the transduction efficiency of the SPAC-seq plasmid

Figure 1. SPAC-seq enables simultaneous CRISPR screening and gene expression profiling on sequencing-based spatial transcriptomic platforms

(A) Schematic of the SPAC-seq workflow.
(B) Plasmid design for SPACseq.
(C) Direct capture of sgRNA used splint-ligated probes compatible with probe-capture-based platforms such as Visium HD.
(D) Capture of sgRNA sequences embedded in mRNA, compatible with poly(dT)-based platforms such as Stereo-seq.
(E) Correlation between genomic and mRNA-embedded sgRNA counts in a mini-pool of 6 sgRNAs targeting 3 genes *in vitro*.
(F) Correlation between genomic and mRNA-embedded sgRNA counts in a large library of 9,040 sgRNAs *in vitro*.
(G) Comparison of correlations between genomic and mRNA-embedded sgRNA counts and between genomic and direct-capture sgRNA counts in a 70-sgRNA library *in vitro*.
(H) Schematic of an *in vivo* CRISPR screen with 1,520 sgRNAs using MC38-Cas9 cells.
(I) Correlation between genomic and mRNA-embedded sgRNA counts for different mouse replicates in the *in vivo* CRISPR screen described in (H) ($n = 5$).
(J) Correlation between genomic DNA- and mRNA-embedded sgRNA counts in 1,520 sgRNAs *in vivo*, pooled with all 5 mice described in (I).
(K and L) Spatial visualization of gene expression (K) and sgRNA library distribution (L) from the CRISPR screen described in (H).
(M) Distribution of spatially sequenced sgRNA counts across various resolutions of bins.
(N) Number of input and recovered sgRNA types, comparing direct-capturing and poly(dT) capturing for embedded mRNA and strategies.
(O) Number of shared sgRNAs captured by direct-capture SPAC-seq and mRNA-embedding SPAC-seq.
(P) Illustration of the multiple sectioning strategy of the SPAC-seq dataset.
(Q) Spearman's correlation of different perturbations across multiple sections at the sgRNA level, with all p values $< 1 \times 10^{-10}$.
(R) Distribution of cells containing different numbers of sgRNAs using the cell bin (8 μm) based approach for the first section (subQ-1) of SPAC-seq.
(S) Spatial visualization of the top 50 perturbations' count, labeled by different colors.
(T) Single-cell segmentation-based visualization of a whole section H&E image (left) and of different ROIs with the top 50 perturbations' count, labeled by different colors (right).
Data are represented as mean ± SEM (G) or box (M, N, and R). *$p < 0.05$, **$p < 0.01$, ***$p < 0.001$, and ****$p < 0.0001$ by unpaired Student's t test (G). ns, not significant. Data are representative of at least two independent experiments (E–G, I, and J).
See also Figure S1 and Tables S1 and S2.

Please cite this article in press as: Zhang et al., Uncovering spatially resolved functional genomics with CRISPR screen sequencing, Cell (2026), https://doi.org/10.1016/j.cell.2026.04.049

system across multiple cell types, including primary T cells (Figures S1A–S1D). This system was benchmarked against the CROPseq plasmid, which is the most widely used sgRNA-embedding for coupling CRISPR perturbations to mRNA capture in single-cell CRISPR screens.[13,18,19,21,33] Key differences between the SPACseq and CROPseq library systems include the use of a retroviral vector optimized for transduction of mouse immune cells and cell lines instead of lentivirus, as well as enhanced transcriptional activity driven by the retroviral long terminal repeat (LTR).[27,28] Notably, the SPACseq plasmid system exhibited significantly higher transduction efficiency across all tested cell types, including the MC38 tumor cell line and primary mouse CD8$^+$ T cells (Figures S1A–S1D). Next, we evaluated the gene knockout (KO) efficiency of SPAC-seq by targeting *Cd8a* in OT1-Cas9 T cells. The SPACseq plasmid achieved a mean KO efficiency of 75.19%, comparable to the efficiencies reported for plasmids used in traditional CRISPR screens,[10,12,15,34] although slightly lower than that of CROP-seq (85.2%) (Figure S1E). This difference is consistent with the dual-sgRNA cassette design used by CROP-seq, which can increase KO efficiency.[13] Additionally, SPACseq plasmid showed robust and consistent genomic perturbation in OT1-Cas9 T cells (Figure S1F).

Traditional CRISPR screens detect sgRNA libraries through genomic DNA sequencing, whereas spatial CRISPR screens rely on transcript detection through spatial transcriptomics, which is prone to substantial dropout.[5] To assess mRNA-embedded sgRNA expression levels, we performed qPCR on mRNA-embedded sgRNA and found that the SPAC-seq system showed 9.08-fold higher expression of mRNA-embedded sgRNA than the CROP-seq system (Figure S1G). This was further supported by the higher median fluorescence intensity (MFI) of the GFP marker, encoded by the same mRNA-sgRNA transcript (Figure S1H). To evaluate the accuracy of sgRNA detection, we compared traditional genomic DNA sequencing with mRNA-based sgRNA capture in SPAC-seq. Using a mini-pool sgRNA library in mouse primary CD8$^+$ T cells, we observed a near-perfect correlation between the two methods (Pearson's correlation, $\rho = 0.9970$, $p < 0.0001$) (Figure 1E), significantly outperforming the CROP-seq system ($\rho = 0.8913$, $p = 0.0046$) (Figure S1I). To further validate this, we analyzed a larger library containing 9,040 sgRNAs in primary CD8$^+$ T cells (Table S1). Despite the increased complexity, SPAC-seq maintained a high correlation with genomic DNA sequencing ($\rho = 0.9414$, $p < 1.0 \times 10^{-32}$) (Figure 1F), demonstrating its scalability and reliability. Additionally, we compared probe-based direct-capture SPAC-seq with traditional genomic DNA sequencing using a mini-pool library of 70 sgRNAs (Table S1). Both mRNA-embedding ($\rho = 0.9796$, $p < 1.0 \times 10^{-48}$) and probe-based direct-capture ($\rho = 0.9596$, $p < 1.0 \times 10^{-38}$) approaches showed strong concordance with genomic DNA sequencing (Figure 1G), confirming the robustness of SPAC-seq for spatial CRISPR screens.

To validate the SPAC-seq system *in vivo*, we performed a CRISPR screen in MC38-Cas9 subcutaneous (subQ) tumors, targeting 735 gene perturbations with 1,520 sgRNAs, including 50 non-targeting control sgRNAs (Figure 1H). The targeted genes encompassed highly expressed tumor membrane proteins, metabolic genes, and immune-related genes (Table S1). Next, we assessed the consistency between traditional genomic DNA sequencing and SPAC-seq's mRNA-embedding sequencing. Across biological replicates, the correlation between these two readouts remained consistently high ($\rho = 0.9464$, $p < 1.0 \times 10^{-32}$) (Figures 1I and 1J), reinforcing the reliability of mRNA-based sgRNA detection. This high correlation persisted when analyzing log2FC for perturbations' growth advantage *in vivo* versus *in vitro* ($\rho = 0.6393$, $p < 1.0 \times 10^{-91}$) (Figure S1J). To further confirm the robustness of gene discovery, we examined the top depleted hits from the *in vivo* tumor screen. The most significantly depleted genes were enriched for major histocompatibility complex (MHC) presentation pathways, which were reported by previous *in vivo* CRISPR screens for tumor cells,[35,36] including *H2-T23*, *B2m*, *H2-K1*, *Ifngr2*, and *H2-Q7* (Figure S1K; Table S2). Additionally, we identified *B4galt1* as a top hit and validated its function in both *in vitro* killing assays and *in vivo* tumor growth models (Figure S1L and S1M), further demonstrating the reliability of SPAC-seq for identifying functionally relevant gene targets.

After validating SPAC-seq's performance in sgRNA library construction, transduction, editing, expression, and sequencing fidelity, we applied it to *in vivo* CRISPR screens in MC38 tumor models. Using the 1,520-sgRNA library, we evaluated both direct capture and mRNA-embedding methods on two spatial transcriptomics platforms, Visium HD[25] and Stereo-seq,[26] both of which were reported to achieve single-cell resolution. Spatial sequencing successfully captured both whole-transcriptome gene expression (Figure 1K) and the sgRNA library (Figure 1L) across both platforms. Comparison of unique molecular identifiers (UMIs) per spatial bin revealed similar distributions between the mRNA-embedding and direct-capture methods, with both achieving approximately 0.8–1 UMI per 8 or 10 μm bin (Figure 1M), indicating comparable efficiency across platforms. Spatial sgRNA counts showed a significant correlation with tissue-level NGS results for both direct-capture SPAC-seq ($\rho = 0.28$, $p < 0.0471$) and mRNA-embedding SPAC-seq ($\rho = 0.47$, $p < 0.6090 \times 10^{-3}$) (Figure S1N). SPAC-seq recovered 1,393 (91.64%) and 1,161 (76.38%) out of 1,520 sgRNAs per tumor section, using direct capture and mRNA embedding, respectively (Figure 1N). Among all captured sgRNAs, 1,068 out of 1,520 (70.26%) sgRNAs were consistently detected by both methods and across tumors from different mice (Figure 1O), demonstrating the high-throughput capacity and efficient sgRNA capture of SPAC-seq.

To further evaluate the technical robustness of SPAC-seq, we performed SPAC-seq profiling on serial sections from the same tumor (Figure 1P) and systematically assessed sgRNA detection, assignment accuracy, and cellular resolution. First, an average of 1,172 out of 1,520 sgRNAs were detected per section, with 934 out of 1,520 (61.45%) sgRNAs consistently captured across all five sections (Figure S1O). Second, both sgRNA-level and gene-level counts were highly correlated across the five sections ($p < 1.0 \times 10^{-300}$), with all pairwise Spearman correlation coefficients exceeding 0.92 (Figures 1Q and S1P). Third, we evaluated the unambiguous assignment of sgRNAs at both the cell-bin (8 μm) and single-cell levels. An 8–10 μm bin size has been reported as a suitable resolution for analyzing the cellular transcriptome in spatial transcriptomics.[37,38] At the cell-bin level,

Please cite this article in press as: Zhang et al., Uncovering spatially resolved functional genomics with CRISPR screen sequencing, Cell (2026), https://doi.org/10.1016/j.cell.2026.04.049

CellPress
OPEN ACCESS

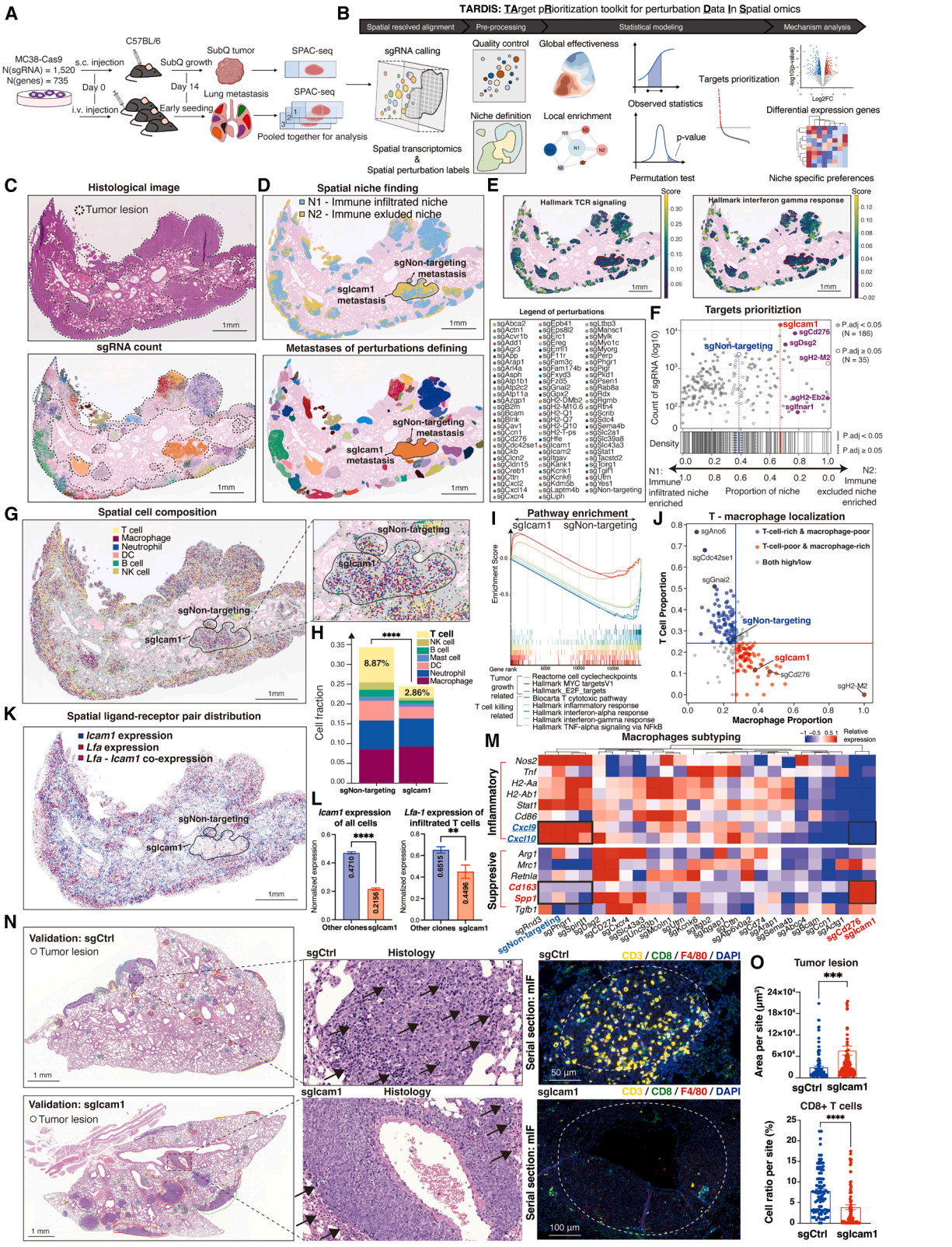

(legend on next page)

Please cite this article in press as: Zhang et al., Uncovering spatially resolved functional genomics with CRISPR screen sequencing, Cell (2026), https://doi.org/10.1016/j.cell.2026.04.049

221,766 out of 632,032 bins (35.09%) were assigned with a single unambiguous sgRNA, corresponding to an average coverage of 145.9 cells per sgRNA across the 1,520 perturbations (Figure 1R). Spatial visualization of sgRNA counts further confirmed the distinct spatial distributions of different perturbations (Figure 1S). To assess the single-cell resolution, we applied StarDist[39,40] to segment cell boundaries and assign RNA reads to individual cells (Figure 1T). Using this approach, 604,139 out of 632,355 sgRNA counts (95.54%) were successfully assigned to segmented single-cell boundaries (Figure S1Q), and 91,825 out of 205,974 cells (44.58%) were detected with a single unambiguous sgRNA (Figure S1R). Among these unambiguous sgRNA cells, 1.51 sgRNA UMIs were detected per single cell (1.27 UMIs per cell bin) (Figure S1S), demonstrating robust single-cell-level perturbation assignment. Together, these benchmarking results demonstrate the potential of SPAC-seq to enable single-cell-resolved spatial CRISPR screens.

Last, we sought to assess the spatial stochasticity of sgRNAs. First, spatial tumor niches represent functionally distinct phenotypes of spatially clustered cells.[41–44] Using CellCharter,[43] we identified six tumor niches (N1–N6) (Figure S1T). The median Pearson's correlations for sgRNAs and perturbations' niche proportions across 5 sections were 0.5613 and 0.6635 (Figure S1U), indicating a conserved localization and related spatial functional phenotypes of sgRNAs and perturbations. Second, we found that 943 out of 1,520 sgRNAs (62.04%) and 632 out of 736 gene perturbations (85.87%) were significantly spatially consistent (false discovery rate [FDR] < 0.05) across sections (Figures S1V and S1W), with a median structural similarity index measure (SSIM) of 0.9995 for sgRNA level and 0.9809 for perturbation level (Figure S1V). These quantifications showed high consistency of the majority of perturbations in the 3-dimensional space.

In summary, our systematic evaluations spanning plasmid design, sequencing performance, spatial reproducibility, and *in vivo* validation collectively demonstrate the robustness of SPAC-seq as a platform for high-throughput spatial CRISPR screening.

Spatial metastasis screen reveals the role of TCR co-stimulation in tumor surveillance

Pooled CRISPR screens have been widely used to identify genes involved in tumor metastasis.[34,45,46] To further demonstrate the utility of SPAC-seq, we applied it to study early stages of tumor metastasis, focusing on tumor cell seeding and interactions with the local microenvironment. MC38-Cas9 cells were transduced with the same 1,520 sgRNA library used in the subcutaneous screen (Table S1), followed by intravenous injection into immunocompetent mice, and lung metastases were harvested for analysis 14 days later (Figure 2A). In total, we recapitulated 952 out of 1,520 sgRNAs (62.23%), with an average of 612.33 sgRNAs per tumor section (Figures S2A and S2B). To analyze this high-dimensional data, we developed TARDIS (target prioritization toolkit for perturbation data in spatial omics), a statistical toolkit to analyze spatial transcriptomics with perturbations (Figure 2B). TARDIS enables spatial alignment of sgRNA reads with the transcriptome, preprocessing of spatial sgRNA libraries, statistical modeling to assess both global effects and local perturbation enrichments, and downstream spatial pathway analysis. Detailed modeling rationale, benchmarking experiments, and validations are provided in the STAR Methods and Figures S11–S18.

As expected, sgRNA counts were predominantly localized within tumor lesions rather than the surrounding lung tissue (Figures 2C and S2C). Most metastases were associated with single perturbations, suggesting local expansion after seeding. The top sgRNAs enriched in lung metastasis relative to primary tumors were also among the top hits when compared with *in vitro* culture (Figure S2D), indicating strong selective pressures in the lung metastatic niche. GO (Gene Ontology) term enrichment analysis of top metastasis-enriched hits revealed significant enrichment of antigen processing and presentation pathways (Figure S2E). Our analysis also demonstrated strong reproducibility, with sgRNAs targeting the same gene consistently recapitulated across targets (Figure S2F) and biological replicates (Figure S2G),

Figure 2. Spatial metastasis screen reveals that loss of TCR co-stimulation promotes tumor colonization and immune exclusion

(A) Schematic of the pooled spatial CRISPR screen to study lung metastasis at the spatial level.
(B) Schematic of TARDIS.
(C) The representative H&E image of tumor lesions (top) and the corresponding spatial CRISPR sgRNA library counts (bottom).
(D) Labeling of perturbations formed the local expansion area (bottom) and their associated TME niches identified by spatial transcriptomics (topl).
(E) Visualization of the top differentially expressed pathways in the immune exclusion niche N2.
(F) Dot plot (upper) and density plot (lower) of enrichment and statistical test of all perturbations across immune-infiltrated and excluded niches.
(G) Spatial visualization of immune cell composition in metastases of perturbations.
(H) Proportions of infiltrated immune cell types in metastases comparing sgIcam1 perturbation and the sgNon-targeting control.
(I) GSEA results for metastases derived from sgIcam1 compared with non-targeting control.
(J) Levels of macrophage and T cell infiltration across different perturbed tumor metastases.
(K) Spatial distribution of *Icam1* and *Lfa-1* gene expression and co-expression (binary).
(L) Statistical analysis of *Icam1* expression of all cells (left) and of *Lfa-1* expression of only T cells infiltrated in metastases (right), comparing sgIcam1 and all other perturbations on the same section.
(M) Expression of inflammatory and suppressive marker genes on macrophages in metastases of the top expanded perturbations.
(N) Representative serial sections of H&E and mIF images of sgCtrl and sgIcam1 perturbation tumor metastases for validating lung metastasis and immune exclusion phenotypes, with lymphocytes indicated by arrows.
(O) Statistical analysis of metastasis tumor area across different tumor lesions (upper) and of the proportion of $CD3^+$ $CD8^+$ T cells to all cells across different tumor lesions (lower).
Data are represented as a box (H) or mean ± SEM (O and L). $^*p < 0.05$, $^{**}p < 0.01$, $^{***}p < 0.001$, and $^{****}p < 0.0001$ by chi-square test (F), unpaired Student's *t* test (L and O), or Pearson's chi-square test (H). ns, not significant. Data are representative of at least two independent experiments (O).
See also Figures S2 and S3 and Tables S1 and S3.

Please cite this article in press as: Zhang et al., Uncovering spatially resolved functional genomics with CRISPR screen sequencing, Cell (2026), https://doi.org/10.1016/j.cell.2026.04.049

reinforcing the reliability of the screen in identifying metastasis-related genes.

To explore tumor spatial clonality, phenotypes, and associated pathways for different perturbations, we first defined locally expanded metastatic regions using DBSCAN (see STAR Methods; Figure 2D, bottom).[16,17,47] We identified 368 sgRNAs that formed 290 metastasis clones, corresponding to 221 gene perturbations (Figures 2D and S2C). We applied CellCharter to further categorize the tumor regions of these perturbation clones into immune-infiltrated (N1) and immune-excluded (N2) niches (Figure 2D, top). Gene set enrichment analysis (GSEA) results of the niches showed distinct immune signatures, including T cell receptor (TCR) signaling and interferon signaling pathways (Figure S2H). Spatial visualization of TCR signaling and interferon-γ (IFN-γ) response pathways revealed that immune infiltration and exclusion phenotypes aligned with niche distribution and specific perturbations (Figure 2E), emphasizing the interplay between perturbations and microenvironmental adaptations. Note that sgNon-targeting replicates were enriched in the immune-infiltrated niche ($p = 0.032$), with an average proportion of 70.13% (Figure S2I). This non-random distribution marks sgNon-targeting as a reliable baseline for other gene perturbations.

Using TARDIS, we identified 138 and 48 out of 221 clonal perturbations as significantly enriched in immune-infiltrated and immune-excluded niches, respectively (Figure 2F; Table S3). Notably, *Icam1*-perturbed tumor cells were both highly expanded and significantly enriched in immune-excluded niches (Figures 2F and S2J). ICAM-1 is a key ligand that interacts with LFA-1 on T cells and enhances TCR stimulation by regulating the tumor-T cell immune synapse.[48–52] Similarly, perturbations of genes involved in MHC signaling and TCR co-stimulation were significantly enriched in the immune-excluded niche, such as *H2-Eb2*, a gene well-characterized in the MHC class 2 complex, and *Cd276*, which has been implicated as a ligand for TCR co-stimulation.[53] These suggest a complex interplay between metastatic tumor regions and the local immune infiltration. We observed a mean similarity of 0.77 for the perturbations' niche distributions, as measured by the cosine similarity (Figure S2K), confirming the reproducibility of biological and spatial enrichment across perturbations. Next, we examined the spatial localization and cell-type composition of the tumor region with different perturbations (Figures 2G and 2H). Notably, the sgIcam1 tumor region exhibited a significantly different immune composition ($p < 0.0001$) (Figure 2H), including the exclusion of T cells (Figure S2L). To further validate these findings, we performed multiplexed immunofluorescence (mIF) on an adjacent section and confirmed the differential distribution of T cells and macrophages in the sgIcam1 metastasis site (Figure S2M).

To further investigate the interaction between tumor perturbations and their corresponding TME, we identified six distinct TME gene programs (Figure S3A; see STAR Methods). GSEA results revealed that program 2 was associated with cell cycle regulation, TCR signaling, and immune cell differentiation, whereas programs 5 and 6 were linked to tumor cell growth and showed depletion of TCR signaling (Figure S3B). sgRNA enrichment analysis confirmed that programs 2, 5, and 6 were specific to tumor perturbations (Figure S3C). Spatial mapping showed that the sgIcam1 tumor region was significantly enriched in program 6 ($p < 0.0001$) while being depleted in program 2 ($p < 0.05$) (Figures S3D–S3F), indicating a TME that suppresses immune activation while favoring tumor cell division (Figure S3G). These results suggest that the loss of *Icam1*, the key ligand involved in immune synapses,[48–52] promotes an immune-suppressive microenvironment and enhances tumor proliferation. Further GSEA results comparing sgIcam1 perturbation to the sgNon-targeting control revealed upregulation of pathways related to cell division and tumor growth and downregulation of IFN signaling pathways (Figure 2I). This pattern suggests that loss of IFN signaling in the sgIcam1 tumor region exacerbates T cell exclusion and impairs TCR co-stimulation, thereby further suppressing immune surveillance and promoting tumor progression.

The sgIcam1 tumor region exhibited a T cell-poor, macrophage-rich phenotype compared with sgNon-targeting (Figure 2J). The *Icam1-Lfa-1* interaction is known to enhance T cell trafficking within tumor cells.[54] We analyzed the spatial co-expression of *Icam1-Lfa-1* and found a significant reduction in *Icam1* expression ($p < 0.0001$) within the sgIcam1 tumor region, alongside decreased *Lfa-1* expression ($p < 0.01$) in infiltrated T cells in this region (Figures 2K and 2L), indicating impaired interactions between cancer cells and T cells. Also, this T cell-poor, macrophage-rich phenotype observed in the sgIcam1 tumor region is associated with immune suppression in lung metastasis, particularly mediated by reduced *Il12* expression.[55] Consistently, we observed reduced *Il12a* expression in the sgIcam1 tumor region (Figure S3H), supporting the presence of a macrophage-driven suppressive microenvironment. To investigate the perturbation's impact on both T cells and macrophages, we analyzed the subtypes of infiltrated immune cells by comparing Icam1 perturbation to the sgNon-targeting controls (Figure S3I). Cytotoxic $CD8^+$ T cells were notably excluded in the *Icam1*-perturbed tumor region (Figure S3I), while M2-like macrophages, known for suppressing cytotoxic $CD8^+$ T cells,[56] were increased in the *Icam1*-perturbed tumor region, suggesting an immune-suppressive polarization in macrophages that disrupts $CD8^+$ T cell immunity. Further analysis of macrophage polarization revealed that inflammatory markers such as *Cxcl9* and *Cxcl10* were enriched in the sgNon-targeting tumor regions, whereas suppressive markers such as *Spp1* and *Cd163* were elevated in the sgIcam1 tumor region (Figure 2M). To validate these findings, we intravenously injected MC38-Cas9 tumor cells perturbed at the *Icam1* or intergenic control (sgCtrl) loci and performed hematoxylin and eosin (H&E) and mIF staining on serial sections for $CD8^+$ T cells and $F4/80^+$ macrophages in lung metastases. Consistently, we confirmed increased $CD8^+$ T cell exclusion phenotypes observed in SPAC-seq (Figure 2N). By analyzing tumor areas in each single metastasis site confirmed by H&E, we found that the tumor area was significantly increased ($p < 0.001$) upon *Icam1* perturbation compared with sgCtrl (Figures 2N and 2O). In addition, we validated that the proportion of T cell infiltration significantly decreased at the single metastasis site level upon *Icam1* perturbation compared with sgCtrl (Figure 2O). Moreover, analysis of the macrophage-to-$CD8^+$ T cell ratio confirmed the T cell-poor, macrophage-rich phenotype in *Icam1* perturbation compared with sgCtrl

Please cite this article in press as: Zhang et al., Uncovering spatially resolved functional genomics with CRISPR screen sequencing, Cell (2026), https://doi.org/10.1016/j.cell.2026.04.049

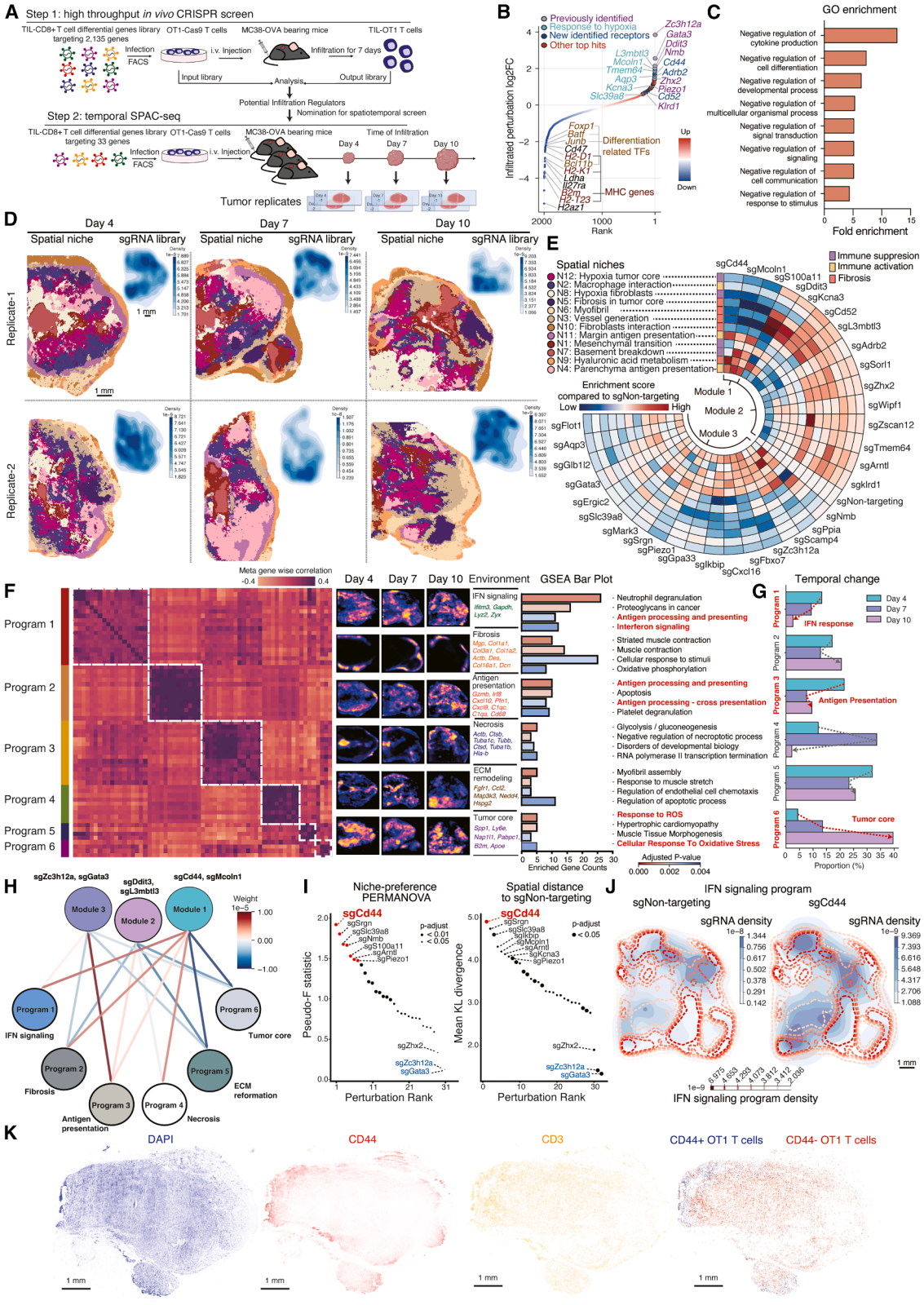

(legend on next page)

Please cite this article in press as: Zhang et al., Uncovering spatially resolved functional genomics with CRISPR screen sequencing, Cell (2026), https://doi.org/10.1016/j.cell.2026.04.049

(Figure S3J). Together, these results validated that perturbing *Icam1* increased the advantage for tumor cells during metastasis seeding and immune surveillance escape.

Spatiotemporal T cell screen reveals the role of CD44 in regulating T cell localization

To understand how T cell-intrinsic states interact with environmental stimuli to influence their spatial localization and function within tumors,[57] we utilized SPAC-seq to identify functional genes that govern $CD8^+$ T cell intratumor localization. We implemented a two-step screening strategy to compress the CRISPR library for $CD8^+$ T cells. First, we conducted an unbiased bulk *in vivo* infiltration screen to identify gene targets whose loss-of-function would enhance T cell infiltration (Figure 3A). Next, we performed an *in vivo* spatiotemporal CRISPR screen using a mini-pool library of the top hits identified in the first step, thereby dissecting the temporal and spatial dynamics of T cell localization within the TME (Figure 3A).

To prepare gene targets for the first-step *in vivo* $CD8^+$ T cell infiltration screen, we analyzed bulk RNA sequencing (RNA-seq) data and scRNA-seq data (see STAR Methods),[58–63] prioritizing 2,135 genes with 9,040 sgRNAs (Table S1). Library-transduced OT1-Cas9 T cells were adoptively transferred into MC38-OVA tumor-bearing $Rag1^{-/-}$ C57BL/6 mice for a bulk *in vivo* screen (Figure 3A, step 1), which successfully recovered 9,006 out of 9,040 sgRNAs (99.62%), with >600 cells per sgRNA, ensuring robust results. Using MAGeCK,[64] we identified perturbations enriched in tumor-infiltrating T cells (Figure 3B; Table S4), including positive controls such as *Zc3h12a* (*Regnase-1*),[65] *Gata3*,[66] *Klrd1* (*CD94*),[36] *Ddit3*,[67] *Nmb*,[68] and *Piezo1*,[69] thereby validating the robustness of the screen. GO enrichment analysis of the top hits revealed pathways related to negative regulation of cytokine production, cell differentiation, signal transduction, cell-cell communication, and response to stimulus (Figure 3C), highlighting the role of environmental sensing in $CD8^+$ T cell infiltration and survival.

Building on the first-step bulk *in vivo* screen, we nominated the top 33 hits for a spatiotemporal CRISPR screen, harvesting tumors at days 4, 7, and 10 to capture distinct stages of infiltration (Figure 3A, step 2). SPAC-seq simultaneously sequenced the perturbation library and high-resolution transcriptome from six tumor sections (Figure 3D). Temporal changes in cell composition were assessed, and we found $CD8^+$ T cells expanded between days 4 and 7, followed by a decline between days 7 and 10, while malignant cells exhibited aggressive growth after day 7 (Figure S4A), indicating a shift in the microenvironment from supporting to suppressing $CD8^+$ T cell infiltration. Interestingly, macrophages showed patterns of expansion and contraction similar to those of T cells (Figure S4A), suggesting potential interactions or regulatory relationships between the two cell types.

To investigate whether T cells perturbed with different genes exhibited spatial preferences for different niches in the TME, we defined and annotated 12 spatial tumor niches using CellCharter (Figure 3D). Despite originating from different mice, these niches exhibited similar evolutionary patterns (Figure 3D), with their proportions and positions dynamically expanding or contracting over time. Time-resolved analysis revealed dynamic shifts in niche proportions over the infiltration period (Figure S4B), and immune-activation spatial niches (N2, N4, and N11) decreased between day 7 and day 10, indicating a more suppressive microenvironment in the late stage. The enrichment for T cells was highly conserved over time (Figure S4C), indicating that as the TME evolved, T cells maintained a relatively stable niche preference. To map perturbations to their preferred tumor niches, we clustered sgRNAs by their enrichment across niches and identified three distinct modules with distinct spatial distributions (Figure 3E; see STAR Methods). This confirmed that $CD8^+$ T cell localization is functionally regulated and closely linked to the TME composition.

To further investigate how the local TME signals shape the spatial localizations of perturbed T cells, we identified six major gene programs that represent key biological pathways (Figure 3F; see STAR Methods). These TME programs aligned with previously defined spatial niches (Figure S4D), supporting their biological relevance. Temporal analysis revealed a significant shift during tumor progression, with IFN response and antigen presentation pathways declining while tumor core-associated pathways, including oxidative stress and ROS (reactive oxygen species) response, became increasingly dominant (Figure 3G). This transition suggests a time-dependent progression toward an immune-suppressive TME.

By linking sgRNA-based modules to TME gene programs, we explored spatial pathway-level mechanisms underlying the

Figure 3. Spatiotemporal $CD8^+$ T cell infiltration screen identifies CD44 as a key regulator of T cell spatial localization

(A) Illustration of a two-step CRISPR screen: a bulk *in vivo* T cell infiltration CRISPR screen (step 1), followed by a mini-pool spatiotemporal T cell CRISPR screen (step 2).

(B) Top hits identified from the *in vivo* CRISPR screen in (A, step 1).

(C) GO enrichment analysis of the top hits described in (B).

(D) Niche clustering across six sections collected at three time points, colored by different niches labeled shared with (E), with the density of captured sgRNAs shown in the upper right corner.

(E) sgRNA enrichment scores across different tumor niches compared with non-targeting control.

(F) NMF analysis of spatial gene expression to identify gene programs within the TME (left) and corresponding GSEA results (right).

(G) Temporal changes in the composition of gene programs identified across different time points.

(H) Network visualization connecting sgRNA perturbation modules described in (E) to the gene programs identified in (F).

(I) Ranking plot showing the effects of each perturbation relative to the non-targeting control, based on niche enrichment scores (left) and distance metrics (right).

(J) Spatial localization of sgCd44 OT1 T cells compared with the sgNon-targeting control, along with the spatial distribution of the IFN signaling program (program 1).

(K) mIF imaging of T cells transferred into $Rag1^{-/-}$ mice, comparing the spatial localization of $CD44^+$ OT1 T cells and $CD44^-$ OT1 T cells, quantified by CD44 and CD3.

See also Figure S4 and Tables S1, S4, and S5.

Please cite this article in press as: Zhang et al., Uncovering spatially resolved functional genomics with CRISPR screen sequencing, Cell (2026), https://doi.org/10.1016/j.cell.2026.04.049

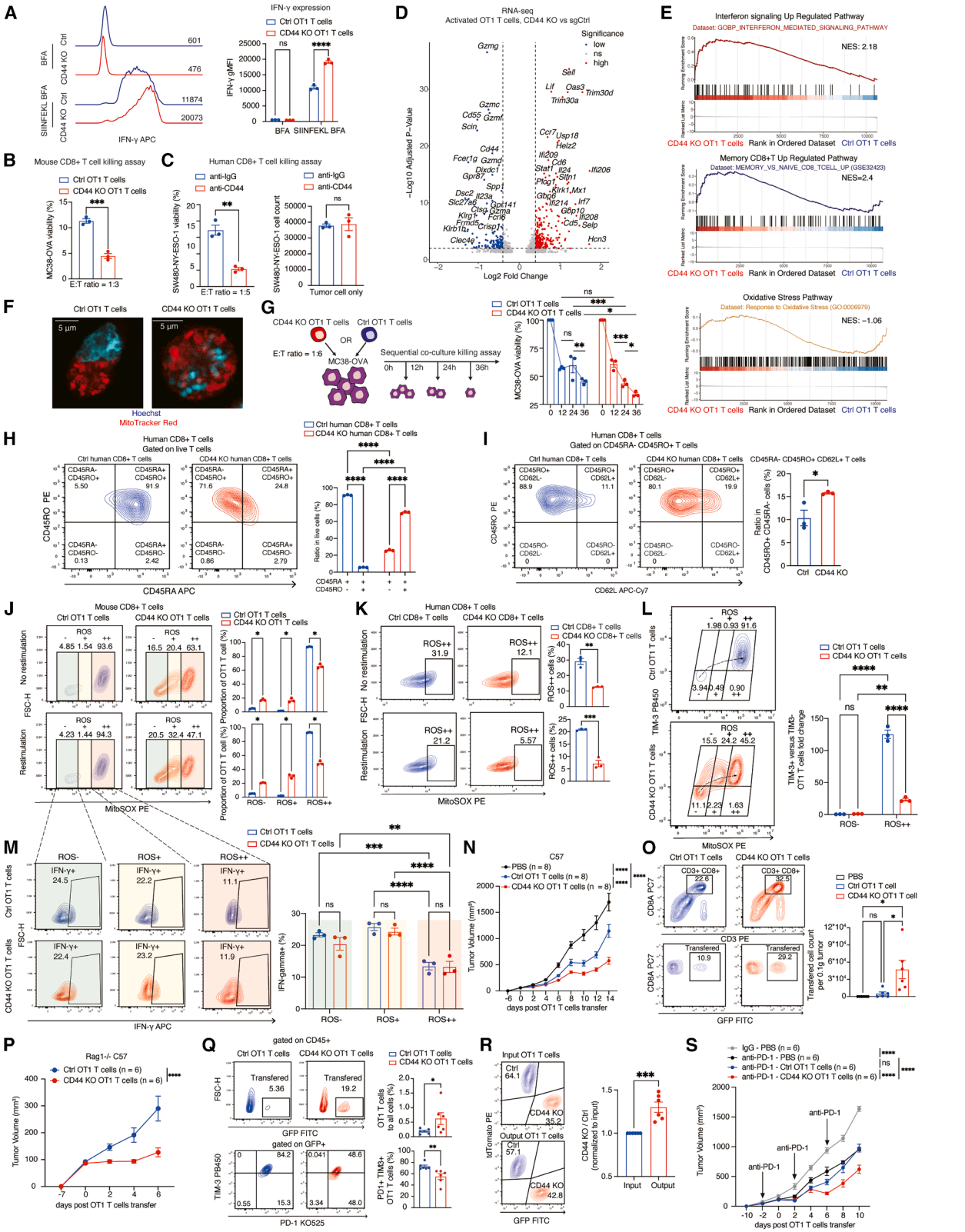

(legend on next page)

Please cite this article in press as: Zhang et al., Uncovering spatially resolved functional genomics with CRISPR screen sequencing, Cell (2026), https://doi.org/10.1016/j.cell.2026.04.049

functional enrichment of specific perturbations (Figure 3H). *Cd44* perturbation, part of module 1, was strongly associated with IFN response (program 1) and antigen presentation (program 3) and negatively correlated with tumor core pathways such as ROS and oxidative stress responses. This pattern suggests that *Cd44*-perturbed OT1 T cells either modulate or selectively localize to microenvironments that enhance IFN signaling while reducing ROS (Figure 3H). Using the TARDIS, we ranked gene perturbations based on their impact on OT1 T cell spatial localization, revealing that *Cd44* perturbation induced the most significant changes in both global localization and local niche preference (Figures 3I and 3J; Table S5). By contrast, perturbation of *Zc3h12a*, a gene reported to regulate T cell-intrinsic pathways,[65] had minimal impact on spatial localization (Figure 3I). This was supported by spatial distributions of sgZc3h12a and sgCd44 relative to non-targeting controls across all tumor sections, confirming consistent localization patterns at both the gene (Figure S4E) and sgRNA levels (Figure S4F). Also, spatial visualization of *Cd44* perturbation confirmed its preference for the IFN signaling pathway compared with the non-targeting control (Figure 3J), indicating increased IFN production in *Cd44*-perturbed OT1 T cells. To validate the spatial localization of *Cd44* perturbation *in vivo*, we co-transferred CD44 KO and CD44$^+$ Ctrl OT1 T cells together into MC38-OVA tumor-bearing Rag1$^{-/-}$ mice. Immunofluorescence staining confirmed the altered localization of CD44-deficient OT1 T cells compared with Ctrl OT1 T cells (Figure 3K). Finally, we analyzed the cell-state phenotypes of sgCd44 OT1 T cells and found that they were predominantly maintained in an effector state over time (Figure S4G). Comparing CD8$^+$ T cell stage proportions between sgCd44 and sgNon-targeting controls revealed that *Cd44* perturbation significantly reduced CD8$^+$ T cell exhaustion (p = 0.032) (Figure S4H), suggesting a functional link between *Cd44*-mediated spatial localization and T cell persistence in the TME.

CD44 restrains CD8$^+$ T cells' anti-tumor immunity by regulating mitochondrial ROS

Given that *Cd44* perturbation promoted CD8$^+$ T cell infiltration into tumors and niches linked to IFN signaling, we hypothesized that *Cd44* restricts CD8$^+$ T cell function, particularly their ability to produce IFN-γ. To test this, we sorted CD44 KO OT1 T cells from all *Cd44*-perturbed OT1 T cells using fluorescence-activated cell sorting (FACS), along with Ctrl OT1 T cells perturbed with sgCtrl (Figure S5A). Upon SIINFEKL (the peptide recognized by OT1) restimulation, CD44 KO OT1 T cells showed a 2-fold increased IFN-γ gMFI (geometric molecular fluorescence intensity) versus controls (Figure 4A). A similar pattern was observed for TNF-α expression (Figure S5B). Additionally, CD44 KO human CD8$^+$ T cells also showed higher IFN-γ under low-dose PMA-ionomycin stimulation (Figure S5C), consistent with mouse OT1 T cells. We next examined CD44 roles in T cell activation and proliferation. Using a CellTrace Violet (CTV) labeled proliferation assay, we found CD44 KO OT1 T cells showed comparable proliferation, as indicated by similar CTV signal decay (Figure S5D). To assess cytotoxicity, we co-cultured CD44 KO or Ctrl OT1 T cells with MC38-OVA tumor cells for 24 h. CD44 KO OT1 T cells exhibited superior killing compared with Ctrl OT1 T cells (Figure 4B). For human CD8$^+$ T cells, anti-CD44 antibody enhanced killing by 1G4 TCR-transduced human CD8$^+$ T cells against NY-ESO-1$^+$ SW480 cells, without affecting SW480 growth alone (Figure 4C).

To investigate the molecular basis of CD44 KO effects, we performed RNA-seq on CD44 KO and Ctrl OT1 T cells co-cultured with MC38-OVA tumor cells and identified differentially expressed genes (DEGs) (Figure 4D; Table S6). Among the top

Figure 4. CD44 restricts T cell anti-tumor immunity by regulating mitochondrial ROS

(A) IFN-γ expression in CD44 KO OT1 T cells compared with control OT1 T cells, measured by gMFI.
(B) Cytotoxicity of CD44 KO and control OT1 T cells co-cultured with MC38-OVA cells.
(C) Cytotoxicity of human CD8$^+$ T cells with 1G4 co-cultured with SW480-NY-ESO-1 cells upon anti-CD44 or anti-IgG treatment (left) and tumor cell count treated with the antibodies only (right).
(D and E) RNA-seq analysis comparing CD44 KO and control OT1 T cells, shown as a volcano plot (D) and as GSEA results for transcriptional signatures of interferon signaling, memory CD8$^+$ T cells, and oxidative stress (E).
(F) Mitochondrial morphology staining in CD44 KO versus control OT1 T cells assessed *in vitro* using MitoTracker and Hoechst.
(G) Temporal killing assay evaluating the long-term killing potential of CD44 KO versus control OT1 T cells.
(H and I) FC analysis (left) with statistical analysis (right) of CD45RO and CD45RA expression (H) and of CD62L (I) for CD44 KO and Ctrl human CD8$^+$ T cells gated on live cells (H) and CD45RA$^-$ CD45RO$^+$ cells (I).
(J and K) FC analysis of mitochondrial ROS levels (left), with a comparison of the frequency of ROS++ level (right) in CD44 KO or control OT1 T cells (J) and in human CD8$^+$ T cells (K).
(L) FC analysis of mitochondrial ROS levels and TIM-3 exhaustion marker expression in CD44 KO versus control OT1 T cells (left), comparing TIM-3 between ROS− and ROS++ groups.
(M) FC analysis of IFN-γ expression levels upon restimulation in CD44 KO versus control OT1 T cells.
(N and O) *In vivo* tumor growth curves in C57BL/6 mice after transferring PBS, control OT1, or CD44 KO OT1 T cells (N) and count of transferred OT1 cells per 0.1 g of MC38-OVA tumors.
(P and Q) *In vivo* tumor growth curves in Rag1$^{-/-}$ C57BL/6 mice after transferring CD44 KO OT1 or control OT1 T cells (P) and frequencies of transferred OT1 T cells to all live cells (upper) and exhausted OT1 T cell frequency to all OT1 T cells (lower) (Q).
(R) Competitive infiltration of CD44 KO (marked with GFP) versus control OT1 T cells (marked with tdTomato) assayed by fold-change of the GFP/tfTomato, normalized to the input.
(S) *In vivo* tumor growth curves in C57BL/6 mice treated with anti-PD1 or anti-IgG and transferred with PBS, Ctrl, or CD44 KO OT1 T cells.
Data are represented as mean ± SEM (A–C and G–S). *$p < 0.05$, **$p < 0.01$, ***$p < 0.001$, and ****$p < 0.0001$ by unpaired Student's t test (B, C, I, K, Q, and R), or two-way ANOVA (A, G, H, J, and L–O). ns, not significant. Data are representative of at least two independent experiments (A–C and F–S).
See also Figure S5 and Table S6.

Please cite this article in press as: Zhang et al., Uncovering spatially resolved functional genomics with CRISPR screen sequencing, Cell (2026), https://doi.org/10.1016/j.cell.2026.04.049

upregulated genes were *Cd62l* (*Sell*) and *Ccr7*, markers of memory T cells, suggesting that CD44 KO T cells acquire a memory-like phenotype. *Oas3*, a key IFN signaling regulator of anti-tumor immunity,[70] was the top upregulated gene. GSEA results confirmed an increase in the IFN-mediated signaling pathway and an enhancement of the memory T cell phenotype in CD44 KO cells (Figure 4E). In addition, RNA-seq of static CD44 KO and Ctrl OT1 T cells, without co-culturing with MC38-OVA tumor cells, revealed significant upregulation of genes linked to T cell stemness and tissue residency, including *Cd103* (*Itgae*), *Tcf7*, *Cd73* (*Nt5e*), *Cd7*, and *Ltb* (Figure S5E; Table S6).[71–73] Notably, *Tim3* (*Havcr2*), a marker of T cell exhaustion, was downregulated in CD44 KO cells. GO analysis revealed positive regulation of IFN-mediated signaling and immunity (Figure S5F). GSEA results verified that gene pathways related to the T cell stem-like stage were upregulated upon CD44 KO (Figure S5G), indicating a benefit of CD44 KO for anti-tumor immunity in adoptive cell transfer (ACT).[74] To validate these findings, we performed flow cytometry (FC) analysis to assess CD62L expression in CD44 KO versus Ctrl OT1 T cells, observing a significant increase in CD62L expression (Figure S5H). To further assess the memory-like phenotype, we stained mitochondria and found that CD44 KO OT1 T cells exhibited a fusion-like mitochondrial distribution, associated with memory-like $CD8^+$ T cells,[75] whereas Ctrl OT1 T cells displayed a fission-like pattern (Figures 4F and S5I). Moreover, time-resolved killing assays showed CD44 KO T cells maintained higher cytotoxicity over 36 h, whereas Ctrl OT1 T cells exhibited a decline in cytotoxicity between 12 and 24 h (Figure 4G), further corroborating the enhanced stemness phenotype and sustained effector function in CD44 KO human $CD8^+$ T cells. The expression of CD45RO, CD45RA, and CD62L, as well-defined markers of memory subtypes,[76] was assessed in CD44 KO versus Ctrl human $CD8^+$ T cells (Figure 4H). We found CD44 KO significantly changed human $CD8^+$ T cells' phenotype from a dominantly $CD45RA^+$ $CD45RO^+$ subset, as intermediate T cells to exhaustion (Tint), to a dominantly $CD45RA^-$ $CD45RO^+$ subset, as either T effector memory (Tem) or central memory (Tcm) subtypes (Figure 4H), suggesting CD44 KO drives T cells to form a stronger memory phenotype. Next, the expression of CD62L was evaluated for $CD45RA^-$ $CD45RO^+$ memory T cells (Figure 4I). Although CD44 KO significantly increased the CD62L+ Tcm subtype, consistent with findings in mouse OT1 T cells (Figure S5H), the majority of memory T cells were enriched in the Tem (effector memory T cell) subtype with low CD62 expression. Together, these results identify Tem as the dominant divergent subset, explaining the memory-like mitochondria and sustained cytotoxicity.

In the RNA-seq data analysis, we also observed a significant downregulation of oxidative stress in CD44 KO T cells (Figures 4D and 4E). Mitochondrial ROS, but not total intracellular ROS, are a well-established indicator of oxidative stress in $CD8^+$ T cells.[77] Elevated mitochondrial ROS level was reported to promote $CD8^+$ T cell death, reflecting accumulated mitochondrial dysfunction and impaired mitophagy.[77] To validate this, we measured mitochondrial ROS levels in OT1 T cells using MitoSOX as a mitochondrial ROS probe. When stratified into low (ROS−), medium (ROS+), and high (ROS++) mitochondrial ROS groups, CD44 KO OT1 T cells exhibited a significantly reduced proportion of ROS++ cells compared with Ctrl T cells, particularly following antigen restimulation (Figure 4J). CD44 KO similarly reduced mitochondrial ROS in human primary $CD8^+$ T cells (Figure 4K). Together, these results suggest that *Cd44* plays a critical role in maintaining elevated mitochondrial ROS levels in T cells. Next, we examined the relationship between ROS levels, T cell exhaustion, and cytokine production. We observed a co-occurrence between expression of exhaustion marker TIM-3 and mitochondrial ROS levels (Figure 4L). This co-occurrence was mitigated in CD44 KO OT1 T cells (Figure 4L). We sorted OT1 T cells by ROS levels and restimulated them to assess IFN-γ production. While IFN-γ levels remained comparable between low- and medium-ROS CD44 KO and Ctrl T cells, they were significantly reduced in the high-ROS group, independent of CD44 status (Figure 4M). These results suggest that the increased IFN-γ production observed in CD44 KO T cells is linked to reduced mitochondrial ROS levels, which may otherwise limit $CD8^+$ T cells' survival after infiltration.

We further evaluated the impact of CD44 KO through *in vivo* ACT assays. First, we transferred CD44 KO or Ctrl OT1 T cells into MC38-OVA tumor-bearing mice. CD44 KO OT1 T cells significantly inhibited tumor growth compared with both PBS control and Ctrl OT1 transfers (Figures 4N and S5J). FC revealed more infiltrated CD44 KO OT1 T cells per 0.1 g tumor (Figure 4O), indicating improved infiltration and intra-tumoral survival. Second, in $Rag1^{-/-}$ mice bearing MC38-OVA tumors, CD44 KO OT1 T cells exhibited superior tumor control (Figure 4P), and FC analysis showed reduced exhaustion of CD44 KO OT1 T cells (Figure 4Q). Third, in a competitive infiltration assay, co-transferred GFP-labeled CD44 KO OT1 T cells consistently outperformed tdTomato-labeled Ctrl OT1 T cells across tumors analyzed (Figure 4R). To further assess therapeutic potential, we combined anti-PD-1 immune checkpoint blockade (ICB) with CD44 KO or Ctrl OT1 ACT. While anti-PD-1 alone initially reduced tumor volume, its efficacy diminished within 7–10 days when combined with Ctrl OT1 ACT (Figures 4S and S5K), aligning with prior observations in the spatiotemporal assay (Figure S4A). By contrast, CD44 KO T cells sustained therapeutic effects throughout the treatment period (Figure 4S). Collectively, these findings demonstrate that CD44 KO enhances $CD8^+$ T cell infiltration, persistence, and tumor control *in vivo*.

SPP1-CD44 axis suppression for $CD8^+$ T cells is abrogated by targeting CD44

To investigate how CD44 KO T cells interact with the local TME, we compared the microenvironment of *Cd44*-perturbed OT1 T cells with Ctrl OT1 T cells using SPAC-seq. DEG analysis revealed significant downregulation of key genes in the TME with CD44 KO T cells compared with sgNon-targeting control, including *Lsr*, *Cxcl14*, and *Spp1* (Figure 5A; Table S7). *Lsr* encodes a lipoprotein receptor reported to interact with and suppress T cells.[78] *Cxcl14*, primarily expressed by fibroblasts,[79] spatially co-localizes with macrophages. *Spp1* is a hallmark of immunosuppressive tumor-associated macrophages that inhibit IFN-γ production in $CD8^+$ T cells.[80–87] Notably, SPP1, as a ligand protein, is well documented to interact with the CD44 receptor.[80,81,88–91] Using the SPAC-seq data, we further identified

Please cite this article in press as: Zhang et al., Uncovering spatially resolved functional genomics with CRISPR screen sequencing, Cell (2026), https://doi.org/10.1016/j.cell.2026.04.049

CellPress
OPEN ACCESS

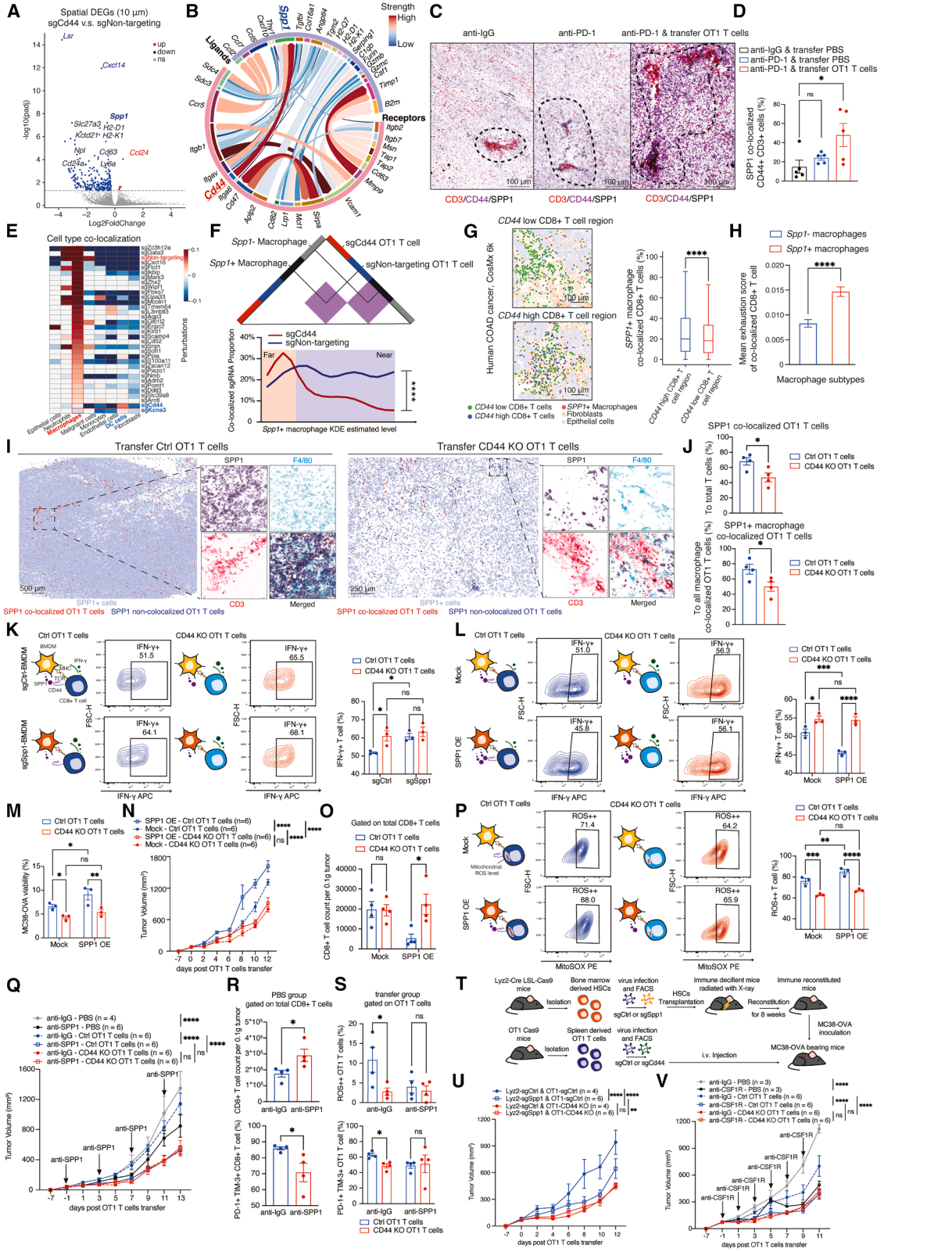

(legend on next page)

Please cite this article in press as: Zhang et al., Uncovering spatially resolved functional genomics with CRISPR screen sequencing, Cell (2026), https://doi.org/10.1016/j.cell.2026.04.049

ligands from other cell types that interact with *Cd44* on T cells, with *Spp1* emerging as the top candidate (Figure 5B). To validate this interaction, we analyzed our Visium HD dataset (Figure 1K) and found that *Spp1*-high regions significantly upregulated T cell marker genes and also genes that were downregulated from CD44 KO OT1 T cells (Figures S6A–S6E; Table S7), suggesting that *Spp1* and *Cd44* co-regulate a shared transcriptional program and that *Spp1*-rich regions are enriched for *Cd44*-expressing T cells. Immunofluorescence staining further confirmed the spatial co-localization of $CD44^+$ T cells with SPP1-expressing cells, which was further enhanced by anti-PD-1 and OT1 T cell transfer treatments (Figures 5C and 5D), indicating the functional relevance of this interaction. Public scRNA-seq datasets revealed high expression of *SPP1* by monocytes/macrophages, particularly post-ICB (Figure S6F).[9] Additional staining confirmed SPP1-co-localizing $CD3^+$ T cells also co-localized with F4/80+ macrophages, indicating that SPP1 interacting with CD44 is related to tumor-associated macrophages rather than tumor cells (Figure S6G).

Next, we analyzed the spatial co-localization of perturbed T cells with other major cell types in the TME. Most perturbed T cells showed strong co-localization with macrophages, while *Cd44*- and *Kcna3*-perturbed OT1 T cells exhibited a unique and significant reduction in co-localization with macrophages (Figure 5E). Notably, *Cd44*-perturbed OT1 T cells were localized significantly farther from *Spp1+* macrophages compared with sgNon-targeting OT1 T cells (Figures 5F and S7A), suggesting a reduced interaction between these *Cd44*-perturbed T cells and *Spp1*+ macrophages. We also validated this interaction using a public spatial transcriptomics dataset of human colon cancer profiled by the CosMx 6K panel (Figures 5G and S7B).[5] Consistent with our mouse data, *CD44*-high human $CD8^+$ T cells were localized closer to *SPP1+* macrophages.[5] Further SPAC-seq analysis revealed that T cells co-localized with *Spp1*+ macrophages were more likely to exhibit an exhausted phenotype (Figure 5H). To validate the SPP1-CD44 axis *in vivo*, we transferred CD44 KO or Ctrl OT1 T cells into $Rag1^{-/-}$ mice bearing MC38-OVA tumors. Immunofluorescence staining for CD3, SPP1, F4/80, and hypoxia probe (pimonidazole HCl) was performed to analyze cell-cell interactions (Figures 5I, 5J, S7C, and S7D). CD44 KO in $CD8^+$ T cells significantly reduced their co-localization with SPP1+ cells, particularly SPP1+ F4/80+ macrophages (Figures 5I, 5J, S7C, and S7D). These findings suggest that the loss of CD44 on T cells disrupts their interaction with immune-suppressive SPP1+ macrophages in the TME. To further validate this interaction at the spatial ligand-receptor level, we applied the proximity ligation assay (PLA) for SPP1 and CD44, combined with mIF on an adjacent section to identify T cells and macrophages (Figures S7E and S7F). We found that regions enriched for $CD3^+$ T cells and F4/80+ macrophages exhibited strong PLA signals for SPP1-CD44 interaction (Figure S7F), confirming macrophage-T cell interactions through SPP1-CD44 at the spatial level.

To investigate the functional role of the SPP1-CD44 axis, we co-cultured CD44 KO and control OT1 T cells with *Spp1*-perturbed or Ctrl BMDMs (bone-marrow-derived macrophages) pulsed with SIINFEKL. FC analysis showed that CD44 KO OT1 T cells exhibited significantly higher IFN-γ production than Ctrl OT1 T cells (Figures 5K, S8A, and S8B). However, this difference diminished when the T cells were co-cultured with *Spp1*-perturbed

Figure 5. Targeting the SPP1-CD44 axis abrogates $CD8^+$ T cell suppression

(A) DEGs between sgCD44 and sgNon-targeting control OT1 T cells that were identified in SPAC-seq.

(B) Ligand-receptor interaction enrichment analysis using the spatial transcriptomics dataset of SPAC-seq. Top ligand-receptors were shown ranked by the corrected area under the precision-recall curve (AUPR) related to T cell activity.

(C) Representative images for mIF of CD3, CD44, and SPP1 staining in MC38-OVA tumors treated with anti-IgG control, anti-PD-1, or anti-PD-1 & transfer OT1 T cells.

(D) Proportion of SPP1 co-localized $CD44^+$ $CD3^+$ cells relative to all $CD3^+$ cells across three treatment groups.

(E) Heatmap showing spatial co-localization of perturbed OT1 T cells (sgRNAs) with other cell types.

(F) Spatial Delaunay triangulation analysis depicting co-localization between perturbed sgCd44 or sgNon-targeting OT1 T cells and $Spp1^+$ or $Spp1^-$ macrophages (upper) and comparison of spatial distances between *Spp1*+ macrophages and sgCd44 versus sgNon-targeting OT1 T cells (lower).

(G) Spatial visualization of co-localization between $SPP1^+$ macrophages and *CD44*-high or *CD44*-low $CD8^+$ T cells, using the CosMx 6K human COAD cancer dataset (see Figure S7B).

(H) Nested bar plot of mean exhaustion scores of OT1 T cells co-localized with $Spp1^-$ or *Spp1*+ of tumor-associated macrophages.

(I and J) Representative mIF images comparing transferred CD44 KO and control OT1 T cells (I) and quantification of SPP1-co-localized and $SPP1^+$ macrophage-co-localized T cells (J) in MC38-OVA tumors from $Rag1^{-/-}$ C57BL/6 mice.

(K and L) FC analysis of IFN-γ expression in CD44 KO versus control OT1 T cells: co-cultured with *Spp1*-perturbed or control BMDMs (K), SPP1 OE, or mock plasmid-expressing BMDMs (L).

(M) Anti-tumor killing assay of CD44 KO versus control OT1 T cells co-cultured with MC38-OVA cells with SPP1 OE or mock plasmid.

(N and O) *In vivo* tumor growth curves of MC38-OVA tumors with SPP1 OE or mock plasmid, with adoptive transfer of CD44 KO or control OT1 T cells (N), and FC analysis of OT1 T cell counts per 0.1 g of tumor in each condition (O).

(P) FC analysis of mitochondrial ROS levels in CD44 KO versus control OT1 T cells co-cultured with SPP1-OE or mock plasmid BMDMs.

(Q–S) Effects of anti-SPP1 or anti-IgG treatment on MC38-OVA tumors with adoptive transfer of CD44 KO or control OT1 T cells: tumor growth curves (Q), FC analysis of mitochondrial ROS and exhaustion levels in all $CD3^+$ $CD8^+$ T cells (R), and mitochondrial ROS level and exhaustion levels in transferred OT1 T cells (S).

(T) Illustration of the *Spp1* cKO experiment.

(U) Tumor growth curves showing effects of cKO of *Spp1* on macrophage for MC38-OVA tumors with adoptive transfer of CD44 KO or control OT1 T cells.

(V) Tumor growth curves showing effects of anti-CSF1R or anti-IgG treatment on MC38-OVA tumors with adoptive transfer of CD44 KO or control OT1 T cells.

Data are represented as a box (G) or mean ± SEM (D, H, J–S, U, and V). $^*p < 0.05$, $^{**}p < 0.01$, $^{***}p < 0.001$, and $^{****}p < 0.0001$ by unpaired Student's *t* test with Welch's correction (F), unpaired Student's *t* test (G, H, J, and R), one-way ANOVA (D), or two-way ANOVA (K–R, U, and V). ns, not significant. Data are representative of at least two independent experiments (K–S and V), except for (U).

See also Figures S6–S9 and Table S7.

Please cite this article in press as: Zhang et al., Uncovering spatially resolved functional genomics with CRISPR screen sequencing, Cell (2026), https://doi.org/10.1016/j.cell.2026.04.049

BMDMs (Figures 5K, S8A, and S8B). Moreover, Ctrl OT1 T cells treated with mouse SPP1 protein (mSPP1) exhibited reduced IFN-γ production with mSPP1, whereas CD44 KO OT1 T cells remained unaffected (Figures S8C and S8D). Similarly, co-culture with SPP1-overexpressing (OE) BMDMs mimicked this suppression in Ctrl but not in CD44 KO OT1 T cells (Figures 5L, S8E, and S8F). To test the potential interaction with tumor cells, we co-cultured CD44 KO and Ctrl OT1 T cells with MC38-OVA cells, either SPP1 OE or with *Spp1* perturbed (Figures S8G and S8H). SPP1 OE suppressed Ctrl OT1 but not CD44 KO OT1 T cells' killing (Figure 5M). This phenotype was further validated by tumor growth curves *in vivo* (Figures 5N and 5O). Interestingly, *Spp1*-perturbed MC38-OVA cells conferred growth advantages regardless of CD44 KO (Figures S8I and S8J), suggesting additional SPP1-mediated pathways in tumor cells. Together, these data reinforced the role of SPP1 in modulating T cell function depending on CD44.

Building on CD44-ROS findings, we co-cultured CD44 KO and control OT1 T cells with SPP1-OE BMDMs or treated them with mSPP1. SPP1-OE BMDMs and mSPP1 both elevated ROS in Ctrl but not in CD44 KO OT1 T cells (Figures 5P and S8K). These results were confirmed by spatial ROS staining in tumors (Figure S7D), supporting SPP1-CD44 regulation of mitochondrial ROS. CD44 has been reported to regulate the uptake of Cu (copper) and Fe (iron) ions, influencing oxidative respiration.[92] Also, high CD44 marks iron-triggered ferroptosis in tumor cells.[93] These reports align well with our RNA-seq findings, which showed significant changes in Fe-related pathways between CD44 KO and Ctrl OT1 T cells (Figure S8L). Using inductively coupled plasma mass spectrometry (ICP-MS),[92] we quantified cellular ion levels (Figures S8M–S8O) and observed that SPP1 treatment significantly increased Fe ions in Ctrl but not in CD44 KO OT1 T cells (Figure S8M). Notably, CD44 KO specifically affected Fe, with no changes in Ca, Mg, Zn, Mn, or Cu (Figure S8N). Prussian blue staining confirmed Fe uptake (as Fe^{3+}) patterns in tumors transferred with CD44 KO or Ctrl OT1 T cells (Figure S7D).[94] Increased Fe and ROS are associated with T cell dysfunction and death,[95–97] supporting a model in which SPP1 suppresses $CD8^+$ T cells through CD44. Notably, Ca influx remained unchanged upon CD44 KO (Figure S8O), suggesting the unaffected TCR signaling mediated by antigen stimulation. As Fe and ROS are ferroptosis markers,[98,99] we investigated SPP1 effects on ferroptosis-regulating proteins NRF2 and GPX4 by western blot (Figure S8P). SPP1 treatment significantly decreased both proteins (normalized to α-tubulin) in controls but not in CD44 KO OT1 T cells, indicating CD44-dependent ferroptosis in $CD8^+$ T cells. As high ROS or low NRF2 inhibits glycolysis,[99] we assayed OT1 T cells' metabolic states with total ATP and lactate production (Figures S8Q and S8R). CD44 KO OT1 T cells showed increased ATP production compared with Ctrl OT1 T cells (Figure S8Q), abrogated by glycolysis inhibitor 2-DG, indicating enhanced glycolysis, as validated by lactate production (Figure S8R). Upon OXPHOS (oxidative phosphorylation) inhibition by oligomycin, glycolysis mildly increased in CD44 KO but decreased in Ctrl OT1 T cells (Figure S8R), indicating that CD44 KO reprogrammed T cells to aerobic glycolysis with reduced OXPHOS dependency.[99–102] Importantly, SPP1 decreased glycolytic capacity in control ($p < 0.01$) but not CD44 KO OT1 T cells. Together, CD44 KO rescues T cells from SPP1-induced inhibition of glycolysis.

Finally, we translated SPP1-CD44 findings into antibody blockade and ACT. We evaluated two clinically relevant antibodies: anti-SPP1[87] and anti-CSF1R,[103] targeting tumor-associated macrophages. Remarkably, anti-SPP1 treatment significantly improved tumor control, reduced $CD8^+$ T cell exhaustion, and lowered mitochondrial ROS levels (Figures 5Q and 5R). Combined with OT1 ACT, anti-SPP1 treatment prevented OT1 T cell exhaustion and significantly decreased mitochondrial ROS levels in the Ctrl OT1 transfer group (Figure 5S). However, these benefits were not significant in the CD44 KO OT1 group (Figure 5S), indicating that the anti-SPP1 treatment effect depends on CD44, further substantiating the role of the SPP1-CD44 axis. To prove that macrophages are indeed a critical source of SPP1, we performed a conditional KO (cKO) *in vivo* assay combined with OT1 ACT for MC38-OVA tumor inoculation (Figure 5T).[104] We found tumor volumes were significantly reduced in comparing *Spp1* cKO and Ctrl mice with Ctrl OT1 T cells transferred but not with CD44 KO OT1 T cells transferred (Figure 5U). Moreover, the *Spp1* cKO abrogated the significant difference of mitochondrial ROS levels between Ctrl and CD44 KO OT1 T cells (Figure S8S), indicating a macrophage-expressed SPP1-dependent effect for OT1 expressing CD44. Additionally, anti-CSF1R treatment attenuated the tumor growth advantage of CD44 KO OT1 T cells while decreasing mitochondrial ROS levels of Ctrl OT1 T cells (Figures 5V and S8T), suggesting that the therapeutic benefits of CD44 KO OT1 T cells are largely dependent on macrophage-mediated suppression. Together, these results demonstrate the potential of treatment targeting the SPP1-CD44 axis to enhance T cell anti-tumor functions.

To assess the human relevance of these findings, we analyzed TCGA-COAD (Colon Adenocarcinoma) data and found that *SPP1* expression strongly correlated with higher ROS levels ($\rho = 0.56$, $p = 8.6 \times 10^{-25}$) (see STAR Methods), increased M2-like macrophage infiltration ($\rho = 0.42$, $p = 9.0 \times 10^{-14}$), and reduced T cell infiltration ($\rho = -0.21$, $p = 2.7 \times 10^{-4}$) (Figure S9A). Importantly, *SPP1* expression was also significantly higher in non-responders receiving ICB treatment (Figure S9B), suggesting a worse treatment response related to *SPP1*. Furthermore, elevated *SPP1* expression combined with macrophage infiltration was associated with worse survival outcomes in COAD patients (Figure S9C). Moreover, co-expression of *CD44* and *SPP1* was associated with poorer survival than *CD44* co-expression with *C1QC* (a marker for less suppressive macrophages) (Figure S9D), highlighting the tumor-promoting role of the *SPP1-CD44* axis in human COAD patients. Overall, our findings highlight the spatially resolved *SPP1-CD44* axis as a key suppressor of $CD8^+$ T cell function within the TME.

Spatially exclusive gene screen reveals $CD8^+$ T cell transcriptional control of chemotaxis

Our findings suggest that $CD8^+$ T cell localization is modulated by environmental cues that alter intrinsic cell states, highlighting a potential interplay between intrinsic cell states and environmental sensing, mediated by exclusively expressed regulators. To explore this, we implemented a two-step screening

Please cite this article in press as: Zhang et al., Uncovering spatially resolved functional genomics with CRISPR screen sequencing, Cell (2026), https://doi.org/10.1016/j.cell.2026.04.049

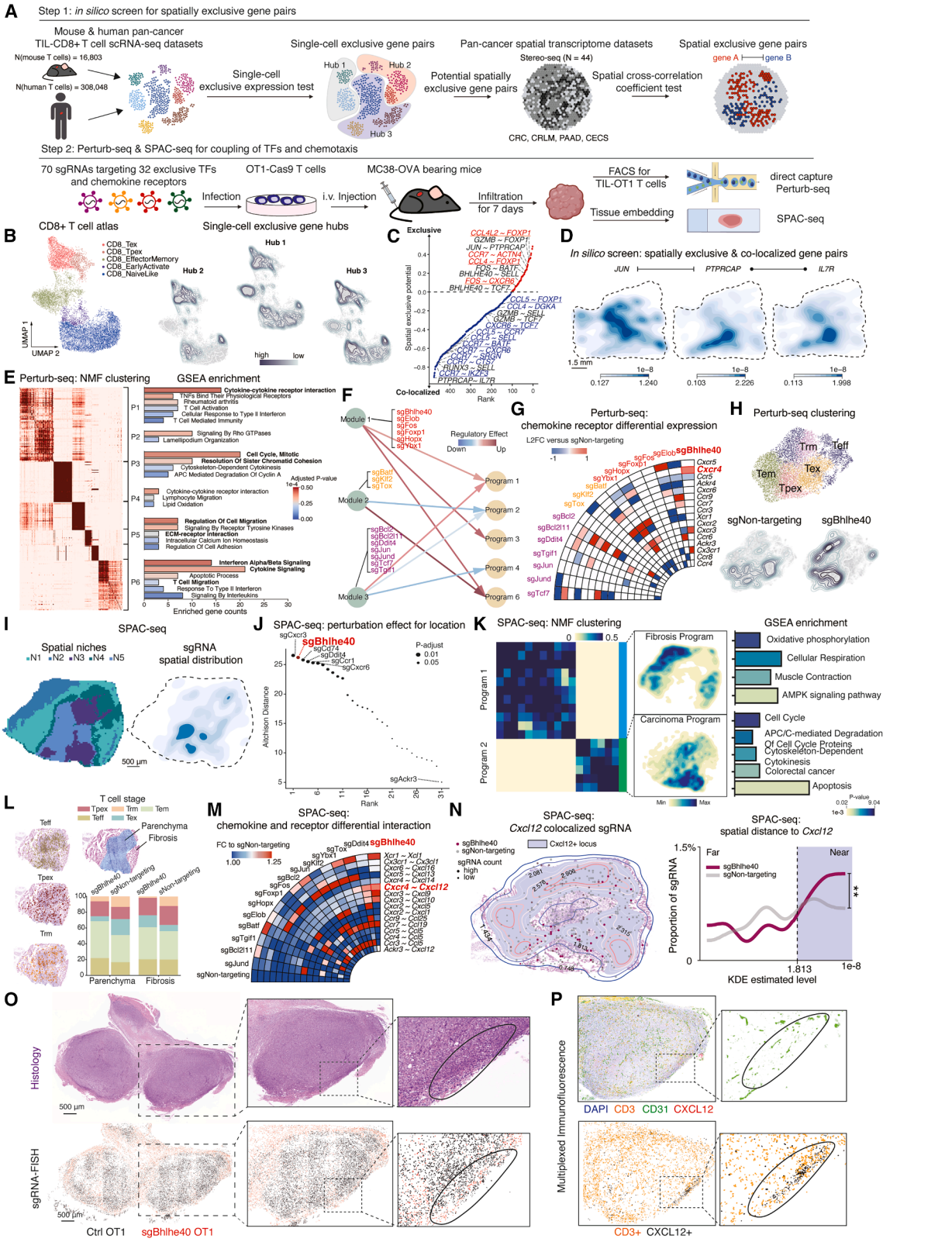

(legend on next page)

Please cite this article in press as: Zhang et al., Uncovering spatially resolved functional genomics with CRISPR screen sequencing, Cell (2026), https://doi.org/10.1016/j.cell.2026.04.049

strategy: an *in silico* screen (Figure 6A, step 1) followed by SPAC-seq analysis (Figure 6A, step 2).

In the *in silico* screen (Figure 6A, step 1), we analyzed over 320,000 human and mouse pan-cancer tumor-infiltrating lymphocyte (TIL)-CD8$^+$ T cells to identify gene pairs with mutually exclusive expression at the single-cell level (see STAR Methods).[105,106] Unbiased single-cell level exclusive gene-expression analysis revealed top exclusive/co-expressed pairs enriched for chemokine receptors and transcription factors (TFs) (Figure S10A; Table S8). Notably, exclusive gene pairs identified in both human and mouse datasets showed a significant correlation (Pearson's r = 0.36, $p < 2.2 \times 10^{-21}$) (Figure S10B), indicating the robustness of the screen. For example, *Cxcr6*, a marker for effector CD8$^+$ T cells, was expressed exclusively with *Tcf7*, a marker for the progenitor-exhausted (Tpex) stage, consistent with previous reports.[107] Hierarchical clustering analysis identified three distinct gene hubs conserved across species (Figure S10C), each closely associated with different CD8$^+$ T cell states (Figures 6B, S10D, and S10E). Among these, a subset of TFs exhibited cell-state-specific expression (Figure S10F), suggesting potential roles in regulating intrinsic cell states and shaping cell-level exclusive gene-expression patterns in CD8$^+$ T cells. SCENIC-based[108] regulatory analysis of these TFs with exclusive gene hubs indicated cell-state-dependent control of gene expression (Figure S10G), reinforcing their roles in shaping state-specific exclusive expression dynamics. We next assessed the spatial exclusivity of genes that passed the single-cell exclusivity test ($n = 477$). Using the pan-cancer spatial transcriptomics datasets (Stereo-seq, $n = 44$), we identified both spatially exclusive gene pairs ($n = 104$) and spatially co-localized gene pairs ($n = 425$) with statistical tests (FDR < 0.05) (Figure 6C). The spatially exclusive genes were enriched in chemotaxis-related genes, such as *CCR7* and *CXCR6*, TFs, such as *TCF7* and *BHLHE40*, and CD8$^+$ T cell-state markers, such as *SELL* (Figures 6C and S10H; Table S8). Visualization of the spatial distribution of top exclusive and co-localized gene pairs (exclusive: *JUN* ~ *PTPRCAP*; co-localized: *PTPRCAP* ~ *IL7R*) validated the results from the *in silico* screens (Figure 6D). These findings indicate that specific TFs and chemokine receptors may regulate both the intrinsic states and spatial positioning of CD8$^+$ T cells, thereby shaping their functional roles and interactions with the environment.

From the *in silico* screens, we nominated the top spatially exclusive TFs, together with CD8$^+$ T cell-expressed chemokine receptors. In total, 70 sgRNAs targeting 32 exclusive TFs and chemokine receptors were pooled together for both the *in vivo* Perturb-seq and SPAC-seq (Figure 6A, step 2; Table S1).

Perturb-seq data, with 6,935 perturbed CD8$^+$ T cells, recapitulated all 70 sgRNAs. Nonnegative matrix factorization (NMF) analysis followed by consensus clustering identified six distinct gene programs annotated with GSEA results (Figure 6E). Among them, programs 1 and 6 were enriched for cytokine-receptor pathways (Figure 6E), suggesting key roles in cell-cell communication via cytokine or chemokine signaling. To link perturbations to gene programs, TF perturbations were clustered into three distinct TF modules based on the transcriptomic change (Figure 6F). Among them, module 1 was positively correlated with cytokine-receptor pathways enriched in programs 1 and 6 (Figure 6F). Expanding on this, we examined how TF perturbations influenced chemokine-receptor expression and found that TF modules exhibited distinct regulatory effects (Figure S10I). Through these perturbation modules, we found sgBhlhe40 notably increased *Cxcr4* expression, and sgCxcr4 perturbation also increased *Bhlhe40* expression (Figures 6G and S10J), suggesting a negative regulatory axis between *Bhlhe40* and *Cxcr4*. Given that BHLHE40 is required for CD8$^+$ T cell tissue infiltration and has been linked to increased exhaustion,[109,110] while CXCR4 promotes CD8$^+$ T cell egress from the tumor parenchyma via its ligand CXCL12,[111] these findings suggest that loss of *Bhlhe40* disrupts intratumoral infiltration by enhancing CXCR4-mediated migration out of the tumor.

Figure 6. Spatially exclusive TF Bhlhe40 regulates CD8$^+$ T cell localization by linking cell state to chemotaxis

(A) Schematic workflow to identify regulators of exclusive programs in CD8$^+$ T cells: step 1, *in silico* screen for spatially exclusive gene pairs; step 2: Perturb-seq and SPAC-seq for top gene pairs.

(B) UMAP plot of different single-cell exclusive gene hubs (right) with different clusters in the mouse CD8$^+$ T cell scRNA-seq atlas (left).

(C) Ranking plot of spatially co-localized and exclusive gene pairs in CD8$^+$ T cells.

(D) Spatial plots of the representative top-excluded gene pair (*JUN* ~ *PTPRCAP*) and the co-localized gene pair (*PTPRCAP* ~ *IL7R*).

(E) Heatmap of NMF analysis results from single-cell Perturb-seq data (left) and associated GSEA results of top pathways (right).

(F) Network diagram showing how perturbation modules connect to gene programs.

(G) Perturbation effects of different TFs (indicated in different colors by modules) on chemokine-receptor expression changes compared with the sgNon-targeting control.

(H) UMAP plot showing cell clusters from the Perturb-seq dataset, highlighting cell stage enrichment of sgBHLHE40 and the sgNon-targeting control.

(I) Spatial plot of the density of captured sgRNAs (right) and spatial niches (left) for the spatial CRISPR screen described in (A, step 2).

(J) TARDIS analysis ranking perturbations that most significantly altered CD8$^+$ T cell location compared with sgNon-targeting controls.

(K) Heatmap of NMF analysis for SPAC-seq dataset (left), corresponding spatial distributions of identified programs (middle), and GSEA results of top pathways associated with each program (right).

(L) Spatial distribution of CD8$^+$ T cells in different cell states (left). Regions defined by H&E annotation (upper right) and box plot comparing *Bhlhe40*-perturbed subtype proportions to sgNon-targeting control (lower right).

(M) Perturbation effects of different TFs on chemokine receptor-ligand pairs, relative to non-targeting.

(N) Spatial distance between sgBhlhe40-perturbed CD8$^+$ T cells and *Cxcl12*, compared with non-targeting T cells (left).

(O and P) H&E images and FISH-IF images of adjacent sections detected with CD3$^+$ sgBhlhe40+ OT1 or CD3$^+$ Ctrl+ OT1 T cells in Rag1$^{-/-}$ mice (O) and adjacent sections for mIF staining showing the spatial distribution of CXCL12+ cells (black) and CD3$^+$ T cells (P).

Data are represented as trend lines (N). *$p < 0.05$, **$p < 0.01$, ***$p < 0.001$, and ****$p < 0.0001$ by unpaired *t* test with Welch's correction (N).

See also Figure S10 and Tables S1, S8, and S9.

Please cite this article in press as: Zhang et al., Uncovering spatially resolved functional genomics with CRISPR screen sequencing, Cell (2026), https://doi.org/10.1016/j.cell.2026.04.049

We next categorized perturbed CD8$^+$ T cells into the following cell states: Tem, Tpex, exhausted (Tex), effector (Teff), and tissue-resident memory (Trm) cells (Figures 6H and S10K). Perturbation effects varied across these states (Figure S10L). Further analysis confirmed that *Bhlhe40* perturbation promoted Teff and Tem states while reducing exhaustion (Figure 6H), indicating its role in balancing effector function and persistence in the TME.

In the SPAC-seq analysis, we identified 5 spatial niches, and a co-localization pattern of sgRNAs was observed within these niches (Figure 6I). A global spatial perturbation effect analysis using TARDIS identified sgCxcr3 and sgBhlhe40 as the top perturbations influencing CD8$^+$ T cell spatial localization compared with the sgNon-tarting control (Figure 6J; Table S9), indicating their significant roles in regulating CD8$^+$ T cell distribution. Notably, most of the top perturbations were chemokine receptors, suggesting CD8$^+$ T cells' spatial localization is regulated by chemotaxis sensing. Next, NMF analysis followed by consensus clustering revealed gene programs associated with fibrosis and tumor parenchyma (Figures 6K and S10M). Spatial mapping of CD8$^+$ T cell subsets (Tpex, Trm, and Tex) revealed distinct spatial localization (Figure 6L). Notably, sgBhlhe40 perturbation increased the representation of the Tem and Tpex subsets while reducing the Tex subset (Figure 6L), consistent with the Perturb-seq dataset (Figure 6H). In addition, CD8$^+$ T cells with sgBhlhe40 perturbation compared with the sgNon-targeting control were enriched in the fibrosis region rather than the parenchyma regions (Figure S10N). We next analyzed the spatial co-localization between TF perturbations and chemokine-receptor loci (Figure 6M). Importantly, sgBhlhe40 perturbation exhibited significantly higher co-localization with the *Cxcl12-Cxcr4* axis compared with control perturbations (Figure 6M). This finding was further supported by the spatial distance between *Cxcl12* and sgBhlhe40, where sgBhlhe40 T cells were more frequently located in close proximity to *Cxcl12* (Figure 6N), suggesting that *Bhlhe40* perturbation enhances chemotaxis sensing and alters the spatial localization of CD8$^+$ T cells within the TME.

To validate these findings, co-transferred sgBhlhe40-perturbed and Ctrl OT1-Cas9 T cells were captured through sgRNA-FISH (fluorescence *in situ* hybridization) (Figure 6O). Consistently, sgBhlhe40-perturbed OT1 T cells were enriched at the tumor's fibrotic margins, as confirmed by histological imaging of adjacent sections (Figure 6O). Moreover, CXCL12+ cells were also predominantly found at tumor margins, where they co-localized with sgBhlhe40-perturbed OT1 T cells (Figure 6P). These support the role of *Bhlhe40* in regulating *Cxcr4* expression, thereby guiding T cell localization through CXCL12 sensing. Additionally, CD31$^+$ cells surrounded both CXCL12+ cells and sgBhlhe40-perturbed OT1 T cells (Figure 6P), suggesting that CXCR4-CXCL12 signaling may facilitate T cell egress via lymphatic vessels.[111] Last, we validated the functional consequences of the change in spatial localization of *Bhlhe40*-perturbed OT1 T cells. In the ACT model, sgBhlhe40 OT1 T cells showed significantly poorer tumor volume control (Figure S10O) yet exhibited a reduced exhaustion phenotype (Figure S10P), consistent with findings from the Perturb-seq and SPAC-seq datasets, suggesting increased intratumor persistence for T cells enriched in tumor margins. Together, these results reveal a previously unrecognized TF-chemokine receptor axis that links intrinsic transcriptional regulation to spatial localization by coupling cell-intrinsic states with environmental chemotaxis cues.

DISCUSSION

The rapid advancement of single-cell spatial transcriptomics platforms has transformed the study of spatially resolved biological processes within the context of tissue organization. In this study, we developed SPAC-seq, a versatile spatial CRISPR screening technology compatible with various high-throughput, high-resolution sequencing-based spatial transcriptomics platforms, including Visium HD[25] and Stereo-seq.[26] The main barriers to integrating spatial transcriptomics sequencing with CRISPR screens include limited sgRNA capture efficiency, high dropout of low-abundance transcripts,[5] and the risk of sgRNA-barcode mismatches due to recombination.[32] To overcome these limitations, we designed SPACseq, a retroviral plasmid that permits high transduction and detection efficiency. SPACseq encodes a single identical sgRNA sequence for both CRISPR/Cas9-mediated perturbation and mRNA-based detection in each cell. Importantly, reliance on mRNA embedding constrains experimental design.[18–22] This limitation is overcome by the direct-capture SPAC-seq strategy, which enables sgRNA detection independently of mRNA embedding. This approach removes a key plasmid design constraint in spatial CRISPR screening, analogous to direct-capture Perturb-seq in single-cell CRISPR screens.[14] Together, these innovations establish SPAC-seq as a scalable framework for spatial CRISPR screening (Table S10).

To provide a tool for analyzing high-dimensional, phenotype-rich spatial perturbation data, we developed TARDIS (https://github.com/zenglab-pku/TARDIS), a comprehensive toolkit designed to analyze spatial CRISPR screen data in conjunction with spatial transcriptomics profiles, including SPAC-seq data. TARDIS is accessible in Python and R, with an easy-to-follow tutorial (https://TARDIS-tutorial.readthedocs.io/en/latest/Tutorial.html) for streamlined implementation. Using SPAC-seq and TARDIS, we conducted multiple functional spatial CRISPR screens with spatially resolved whole-transcriptome readouts. As a proof of concept, we explored diverse biological phenomena, including the local expansion of perturbation formation, T cell infiltration and localization, and tumor cell metastasis, uncovering critical gene pathways, such as ligand-receptor interactions and chemotaxis sensing, that govern these processes.

We applied SPAC-seq and TARDIS to study tumor metastasis and identified *Icam1* as a key regulator of immune surveillance following tumor seeding. Similarly, we previously reported a bispecific antibody drug that engages ICAM1 and LFA-1 to stimulate T cell immunity,[52] highlighting ICAM1 as a promising target. Meanwhile, this study demonstrates SPAC-seq's power to simultaneously uncover tumor targets, map their interactions with immune cells, and reconstruct pathways governing the TME, providing a scalable framework for identifying new immunotherapeutic strategies.

By extending SPAC-seq to mouse primary CD8$^+$ T cells, we performed the first spatiotemporal CRISPR screen and leveraged TARDIS to identify regulators of infiltration across spatial niches and time points. We defined the dynamics of both

time-resolved functional niches and their related gene programs in the TME. In this T cell transfer model, we found that T cells' preference for different tumor niches was relatively conserved over time, rather than changing with the TME. We reasoned that this is because T cells' spatial localization is driven by passive adaptation to environmental cues rather than by active remodeling of the environment. Such a hypothesis could change the perspective on how to remodel the TME more effectively, such as targeting environmental cues themselves, rather than relying solely on T cells for treatment.

With the unique advantage of SPAC-seq to identify perturbation-related environmental cues and the cell-cell interaction axis, we identified SPP1 as one such factor for CD44-expressing T cells. SPP1+ macrophage was well known to suppress $CD8^+$ T cells' anti-tumor immunity.[85] Also, the importance of the CD44-SPP1 interaction was known for tumor cell macrophages,[88] fibroblast macrophages,[81,112] and tumor cell fibroblasts.[113] However, the effects of this interaction for macrophage-T cells remain largely unknown.[114] Meanwhile, although CD44 on $CD8^+$ T cells is well known as a marker with high expression after stimulation, its regulation for effector $CD8^+$ T cells is not well established. Now, this CD44-SPP1 axis provides an alternative explanation for how SPP1+ macrophages suppress T cell immunity.[80,84,85]

Single-cell exclusive genes remain valuable markers of cell states, while spatially exclusive or co-localized genes provide insights into cell positioning and cell-cell communication. We propose a model for T cell localization regulation in which intrinsic cell states are tightly coupled with chemotaxis sensing. This model corroborates prior observations that T cell spatial distributions correlate with their differentiation stages.[107,115] To explore the regulation of $CD8^+$ T cell localization, we integrated an *in silico* screen, a single-cell CRISPR screen (Perturb-seq), and a spatial CRISPR screen (SPAC-seq). We found that *Bhlhe40* perturbation reduced T cell infiltration in the tumor parenchyma and decreased anti-tumor immunity, which contrasts with previous findings linking Bhlhe40 loss to improved anti-tumor immunity from bulk CRISPR screens.[116,117] This discrepancy suggests that conventional CRISPR screens may overlook the impact of T cell localization. Our results highlight the power of spatially resolved CRISPR screens to uncover regulators of T cell function and positioning. By capturing spatial dynamics, this approach provides deeper insights into T cell-mediated immunity and offers a framework for improving ACT and CAR-T therapies. This approach extends to other immune cells, such as macrophages, and can be applied to study spatially resolved functional genomics in diverse tissues and diseases.

With SPAC-seq and TARDIS, we introduce a robust platform for uncovering gene functions at single-cell spatial resolution, establishing a new framework for spatially resolved functional genomics and perturbation analysis. This approach extends beyond T cells, enabling the study of diverse cell types and their spatial behaviors across various biological and pathological contexts. The direct-capture strategy implemented in SPAC-seq would support diverse sgRNA scaffold designs, making it compatible with CRISPRa/i, ORF screens, and other spatially barcoded perturbation strategies. This flexibility expands its applications in functional genomics within complex tissue environments. By integrating spatially resolved gene functions, cell-cell interactions, and dynamic cell states, SPAC-seq and TARDIS provide new opportunities to dissect tissue microenvironments and advance our understanding of spatially regulated biological processes.

Limitations of the study

A limitation of this study is that the KO efficiency of the SPAC-seq plasmid, although comparable to that of plasmids used in traditional CRISPR screens, is lower than that of the dual-sgRNA design in CROP-seq. Therefore, further studies could be conducted to increase the KO efficiency of the SPAC-seq plasmid by inserting a dual-sgRNA cassette that transcribes two sgRNA replicates targeting a single gene. Another limitation of this study is the sequencing depth for both sgRNAs and the transcriptome, constraining deeper single-cell-level analysis of the spatial CRISPR screen. We addressed this problem by assigning perturbations to each cell bin or single cell detected with sgRNAs and analyzing spatial phenotypes using the assigned cells as statistical units rather than sgRNA counts. Also, we developed TARDIS to identify local expanded tumor clones and rescue many undetected cells within their regions. However, despite these efforts, we acknowledge that low sequencing depth remains a limitation. Further development of the spatial sequencing technology would address this limitation by increasing the sequencing coverage.

RESOURCE AVAILABILITY

Lead contact

Requests for further information and resources should be directed to and will be fulfilled by the lead contact, Zexian Zeng (zexianzeng@pku.edu.cn).

Materials availability

Plasmids generated in this study, including SPACseq, are available from the lead contact upon request.

Data and code availability

Spatial transcriptomics datasets, bulk RNA-seq datasets, and Perturb-seq datasets reported in this paper are in GSA (Genome Sequence Archive) under the accession number GSA: CRA023189. The public datasets can be found in the referenced articles. All Jupyter Notebooks or pipeline scripts used to analyze SPAC-seq, Stereo-seq, Visium HD data, and TARDIS benchmark codes are deposited in the repository at https://github.com/zenglab-pku/SPAC-seq. Updated links to the TARDIS packages and tutorials are available at https://TARDIS-tutorial.readthedocs.io/en/latest/Tutorial.html. Processed datasets are also available for viewing, analyzing, and downloading on the SPAC-seq website: https://spac.pku-genomics.org.

ACKNOWLEDGMENTS

This work was supported by the National Natural Science Foundation of China (92374116, 92574301, 32470664, and 82341026), the Beijing Natural Science Foundation (L248043), the Noncommunicable Chronic Diseases-National Science and Technology Major Project (2024ZD0520600), the Innovative Drug Research and Development — National Science and Technology Major Project (2025ZD1800400), the Sichuan Science and Technology Program (2024YFFK0064), the Beijing Advanced Center of Cellular Homeostasis and Aging-Related Diseases, and the Peking-Tsinghua Center for Life Sciences. We thank the Laboratory Animal Center and the National Center for Protein Sciences at Peking University, and we are especially grateful to Dr. Yonglu, Dr. Hongxia Lv, Dr. Chunyan Shan, and Dr. Guilan Li for their technical assistance.

Please cite this article in press as: Zhang et al., Uncovering spatially resolved functional genomics with CRISPR screen sequencing, Cell (2026), https://doi.org/10.1016/j.cell.2026.04.049

AUTHOR CONTRIBUTIONS

Conceptualization, H. Zhang, Z. Zhang, Y.F., D.P., and Z. Zeng; methodology, H. Zhang, Z. Zhang, P.W., Y.F., D.P., and Z. Zeng; software, Z. Zhang, P.W., and H. Zhang; investigation, H. Zhang, Z. Zhang, P.W., T.X., X.C., Yanping Zhao, S.L., W.C., P.R., P.Z., C.L., and Yahai Zhao; visualization, H. Zhang, Z. Zhang, P.W., T.X., S.L., Yanping Zhao, Y.W., and C.L.; funding acquisition, D.P. and Z. Zeng; project administration, Y.F., D.P., and Z. Zeng; supervision, S.H., Yahai Zhao, H. Zeng, Z.L., C.W., Z.G., Y.F., D.P., and Z. Zeng; resources, Z.L. and C.W.; writing – original draft, H. Zhang, Z. Zhang, P.W., Yanping Zhao, and Z. Zeng; writing – review & editing, H. Zhang, Z. Zhang, P.W., H. Zeng, Y. F., D.P., and Z. Zeng.

DECLARATION OF INTERESTS

Z. Zeng, H. Zhang, and Z. Zhang are inventors on a patent application filed by Peking University and Peking University Chengdu Academy for Advanced Interdisciplinary Biotechnologies related to SPAC-seq, as reported in this work. D.P. received sponsored research funding from Bayer AG and Boehringer Ingelheim. These grants were not related to the research reported in this study.

STAR★METHODS

Detailed methods are provided in the online version of this paper and include the following:

SUPPLEMENTAL INFORMATION

Supplemental information can be found online at https://doi.org/10.1016/j.cell.2026.04.049.

Received: April 18, 2025
Revised: January 22, 2026
Accepted: April 30, 2026

REFERENCES

1. Liu, L., Chen, A., Li, Y., Mulder, J., Heyn, H., and Xu, X. (2024). Spatiotemporal omics for biology and medicine. Cell *187*, 4488–4519. https://doi.org/10.1016/j.cell.2024.07.040.
2. Tian, L., Chen, F., and Macosko, E.Z. (2023). The expanding vistas of spatial transcriptomics. Nat. Biotechnol. *41*, 773–782. https://doi.org/10.1038/s41587-022-01448-2.
3. Seferbekova, Z., Lomakin, A., Yates, L.R., and Gerstung, M. (2023). Spatial biology of cancer evolution. Nat. Rev. Genet. *24*, 295–313. https://doi.org/10.1038/s41576-022-00553-x.
4. Bressan, D., Battistoni, G., and Hannon, G.J. (2023). The dawn of spatial omics. Science *381*, eabq4964. https://doi.org/10.1126/science.abq4964.
5. Ren, P., Zhang, R., Wang, Y., Zhang, P., Luo, C., Wang, S., Li, X., Zhang, Z., Zhao, Y., He, Y., et al. (2025). Systematic benchmarking of high-throughput subcellular spatial transcriptomics platforms across human tumors. Nat. Commun. *16*, 9232. https://doi.org/10.1038/s41467-025-64292-3.
6. Wu, L., Jin, Y., Zhao, X., Tang, K., Zhao, Y., Tong, L., Yu, X., Xiong, K., Luo, C., Zhu, J., et al. (2023). Tumor aerobic glycolysis confers immune evasion through modulating sensitivity to T cell-mediated bystander killing via TNF-α. Cell Metab. *35*, 1580–1596.e9. https://doi.org/10.1016/j.cmet.2023.07.001.
7. Mali, P., Yang, L., Esvelt, K.M., Aach, J., Guell, M., DiCarlo, J.E., Norville, J.E., and Church, G.M. (2013). RNA-guided human genome engineering via Cas9. Science *339*, 823–826. https://doi.org/10.1126/science.1232033.

8. Cong, L., Ran, F.A., Cox, D., Lin, S., Barretto, R., Habib, N., Hsu, P.D., Wu, X., Jiang, W., Marraffini, L.A., and Zhang, F. (2013). Multiplex genome engineering using CRISPR/Cas systems. Science *339*, 819–823. https://doi.org/10.1126/science.1231143.

9. Luo, C., Zhang, R., Guo, R., Wu, L., Xue, T., He, Y., Jin, Y., Zhao, Y., Zhang, Z., Zhang, P., et al. (2025). Integrated computational analysis identifies therapeutic targets with dual action in cancer cells and T cells. Immunity *58*, 745–765.e9. https://doi.org/10.1016/j.immuni.2025.02.007.

10. Shalem, O., Sanjana, N.E., Hartenian, E., Shi, X., Scott, D.A., Mikkelson, T., Heckl, D., Ebert, B.L., Root, D.E., Doench, J.G., and Zhang, F. (2014). Genome-scale CRISPR-Cas9 knockout screening in human cells. Science *343*, 84–87. https://doi.org/10.1126/science.1247005.

11. Shi, H., Doench, J.G., and Chi, H. (2023). CRISPR screens for functional interrogation of immunity. Nat. Rev. Immunol. *23*, 363–380. https://doi.org/10.1038/s41577-022-00802-4.

12. Dixit, A., Parnas, O., Li, B., Chen, J., Fulco, C.P., Jerby-Arnon, L., Marjanovic, N.D., Dionne, D., Burks, T., Raychowdhury, R., et al. (2016). Perturb-seq: Dissecting molecular circuits with scalable single-cell RNA profiling of pooled genetic screens. Cell *167*, 1853–1866.e17. https://doi.org/10.1016/j.cell.2016.11.038.

13. Datlinger, P., Rendeiro, A.F., Schmidl, C., Krausgruber, T., Traxler, P., Klughammer, J., Schuster, L.C., Kuchler, A., Alpar, D., and Bock, C. (2017). Pooled CRISPR screening with single-cell transcriptome readout. Nat. Methods *14*, 297–301. https://doi.org/10.1038/nmeth.4177.

14. Replogle, J.M., Norman, T.M., Xu, A., Hussmann, J.A., Chen, J., Cogan, J.Z., Meer, E.J., Terry, J.M., Riordan, D.P., Srinivas, N., et al. (2020). Combinatorial single-cell CRISPR screens by direct guide RNA capture and targeted sequencing. Nat. Biotechnol. *38*, 954–961. https://doi.org/10.1038/s41587-020-0470-y.

15. Zhou, P., Shi, H., Huang, H., Sun, X., Yuan, S., Chapman, N.M., Connelly, J.P., Lim, S.A., Saravia, J., Kc, A., et al. (2023). Single-cell CRISPR screens in vivo map T cell fate regulomes in cancer. Nature *624*, 154–163. https://doi.org/10.1038/s41586-023-06733-x.

16. Dhainaut, M., Rose, S.A., Akturk, G., Wroblewska, A., Nielsen, S.R., Park, E.S., Buckup, M., Roudko, V., Pia, L., Sweeney, R., et al. (2022). Spatial CRISPR genomics identifies regulators of the tumor microenvironment. Cell *185*, 1223–1239.e20. https://doi.org/10.1016/j.cell.2022.02.015.

17. Mollaoglu, G., Tepper, A., Falcomatà, C., Potak, H.T., Pia, L., Amabile, A., Mateus-Tique, J., Rabinovich, N., Park, M.D., LaMarche, N.M., et al. (2024). Ovarian cancer-derived IL-4 promotes immunotherapy resistance. Cell *187*, 7492–7510.e22. https://doi.org/10.1016/j.cell.2024.10.006.

18. Gu, J., Iyer, A., Wesley, B., Taglialatela, A., Leuzzi, G., Hangai, S., Decker, A., Gu, R., Klickstein, N., Shuai, Y., et al. (2024). Mapping multimodal phenotypes to perturbations in cells and tissue with CRISPRmap. Nat. Biotechnol. *43*, 1101–1115. https://doi.org/10.1038/s41587-024-02386-x.

19. Kudo, T., Meireles, A.M., Moncada, R., Chen, Y., Wu, P., Gould, J., Hu, X., Kornfeld, O., Jesudason, R., Foo, C., et al. (2024). Multiplexed, image-based pooled screens in primary cells and tissues with PerturbView. Nat. Biotechnol. *43*, 1091–1100. https://doi.org/10.1038/s41587-024-02391-0.

20. Binan, L., Jiang, A., Danquah, S.A., Valakh, V., Simonton, B., Bezney, J., Manguso, R.T., Yates, K.B., Nehme, R., Cleary, B., and Farhi, S.L. (2025). Simultaneous CRISPR screening and spatial transcriptomics reveal intracellular, intercellular, and functional transcriptional circuits. Cell *188*, 2141–2158.e18. https://doi.org/10.1016/j.cell.2025.02.012.

21. Saunders, R.A., Allen, W.E., Pan, X., Sandhu, J., Lu, J., Lau, T.K., Smolyar, K., Sullivan, Z.A., Dulac, C., Weissman, J.S., et al. (2025). Perturb-Multimodal: A platform for pooled genetic screens with imaging and sequencing in intact mammalian tissue. Cell *188*, 4790–4809.e22. https://doi.org/10.1016/j.cell.2025.05.022.

22. Cheng, Y., Dang, S., Zhang, Y., Chen, Y., Yu, R., Liu, M., Jin, S., Han, A., Katz, S., and Wang, S. (2025). Sequencing-free whole-genome spatial transcriptomics at single-molecule resolution. Cell *188*, 6953–6970.e12. https://doi.org/10.1016/j.cell.2025.09.006.

23. Rong Fan, A.B., Tian, X., et al. (2025). Spatially Resolved Panoramic in vivo CRISPR Screen via Perturb-DBiT. Preprint at Rs. Sq. https://doi.org/10.21203/rs.3.rs-6481967/v1.

24. Shen, K., Seow, W.Y., Keng, C.T., Lim, M.G.L., Lim, D.S., Guo, K., Meliani, A., Irfan Bin Hajis, M., Wang, B., Prabhakar, S., et al. (2026). Spatial perturb-seq: single-cell functional genomics within intact tissue architecture. Nat. Commun. *17*, 3018. https://doi.org/10.1038/s41467-026-69677-6.

25. Oliveira, M.F.D., Romero, J.P., Chung, M., Williams, S.R., Gottscho, A.D., Gupta, A., Pilipauskas, S.E., Mohabbat, S., Raman, N., Sukovich, D.J., et al. (2025). High-definition spatial transcriptomic profiling of immune cell populations in colorectal cancer. Nat. Genet. *57*, 1512–1523. https://doi.org/10.1038/s41588-025-02193-3.

26. Chen, A., Liao, S., Cheng, M., Ma, K., Wu, L., Lai, Y., Qiu, X., Yang, J., Xu, J., Hao, S., et al. (2022). Spatiotemporal transcriptomic atlas of mouse organogenesis using DNA nanoball-patterned arrays. Cell *185*, 1777–1792.e21. https://doi.org/10.1016/j.cell.2022.04.003.

27. Kitamura, T., Koshino, Y., Shibata, F., Oki, T., Nakajima, H., Nosaka, T., and Kumagai, H. (2003). Retrovirus-mediated gene transfer and expression cloning: powerful tools in functional genomics. Exp. Hematol. *31*, 1007–1014. https://doi.org/10.1016/S0301-472X(03)00260-1.

28. Finnegan, D.J. (2012). Retrotransposons. Curr. Biol. *22*, R432–R437. https://doi.org/10.1016/j.cub.2012.04.025.

29. Henriksson, J., Chen, X., Gomes, T., Ullah, U., Meyer, K.B., Miragaia, R., Duddy, G., Pramanik, J., Yusa, K., Lahesmaa, R., and Teichmann, S.A. (2019). Genome-wide CRISPR Screens in T Helper Cells Reveal Pervasive Crosstalk between Activation and Differentiation. Cell *176*, 882–896.e18. https://doi.org/10.1016/j.cell.2018.11.044.

30. Chen, Z., Arai, E., Khan, O., Zhang, Z., Ngiow, S.F., He, Y., Huang, H., Manne, S., Cao, Z., Baxter, A.E., et al. (2021). In vivo CD8+ T cell CRISPR screening reveals control by Fli1 in infection and cancer. Cell *184*, 1262–1280.e22. https://doi.org/10.1016/j.cell.2021.02.019.

31. Kurachi, M., Kurachi, J., Chen, Z., Johnson, J., Khan, O., Bengsch, B., Stelekati, E., Attanasio, J., McLane, L.M., Tomura, M., et al. (2017). Optimized retroviral transduction of mouse T cells for in vivo assessment of gene function. Nat. Protoc. *12*, 1980–1998. https://doi.org/10.1038/nprot.2017.083.

32. Adamson, B., Norman, T.M., Jost, M., and Weissman, J.S. (2018). Approaches to maximize sgRNA-barcode coupling in Perturb-seq screens. Preprint at bioRxiv. https://doi.org/10.1101/298349.

33. Datlinger, P., Pankevich, E.V., Arnold, C.D., Pranckevicius, N., Lin, J., Romanovskaia, D., Schaefer, M., Piras, F., Orts, A.-C., Nemc, A., et al. (2025). Systematic discovery of CRISPR-boosted CAR T cell immunotherapies. Nature *646*, 963–972. https://doi.org/10.1038/s41586-025-09507-9.

34. Chen, S., Sanjana, N.E., Zheng, K., Shalem, O., Lee, K., Shi, X., Scott, D.A., Song, J., Pan, J.Q., Weissleder, R., et al. (2015). Genome-wide CRISPR screen in a mouse model of tumor growth and metastasis. Cell *160*, 1246–1260. https://doi.org/10.1016/j.cell.2015.02.038.

35. Tsao, H.W., Anderson, S., Finn, K.J., Perera, J.J., Pass, L.F., Schneider, E.M., Jiang, A., Fetterman, R., Chuong, C.L., Kozuma, K., et al. (2024). Targeting the aminopeptidase ERAP enhances antitumor immunity by disrupting the NKG2A-HLA-E inhibitory checkpoint. Immunity *57*, 2863–2878.e12. https://doi.org/10.1016/j.immuni.2024.10.013.

36. Dubrot, J., Du, P.P., Lane-Reticker, S.K., Kessler, E.A., Muscato, A.J., Mehta, A., Freeman, S.S., Allen, P.M., Olander, K.E., Ockerman, K.M., et al. (2022). In vivo CRISPR screens reveal the landscape of immune evasion pathways across cancer. Nat. Immunol. *23*, 1495–1506. https://doi.org/10.1038/s41590-022-01315-x.

37. Zhang, D., Schroeder, A., Yan, H., Yang, H., Hu, J., Lee, M.Y.Y., Cho, K.S., Susztak, K., Xu, G.X., Feldman, M.D., et al. (2024). Inferring

super-resolution tissue architecture by integrating spatial transcriptomics with histology. Nat. Biotechnol. *42*, 1372–1377. https://doi.org/10.1038/s41587-023-02019-9.

38. Cho, C.-S., Xi, J., Si, Y., Park, S.-R., Hsu, J.-E., Kim, M., Jun, G., Kang, H. M., and Lee, J.H. (2021). Microscopic examination of spatial transcriptome using Seq-Scope. Cell *184*, 3559–3572.e22. https://doi.org/10.1016/j.cell.2021.05.010.

39. Martin, W., and Uwe, S. (2022). Nuclei Instance Segmentation and Classification in Histopathology Images with Stardist. In 2022 IEEE International Symposium on Biomedical Imaging Challenges (ISBIC), pp. 1–4. https://doi.org/10.1109/ISBIC56247.2022.9854534.

40. Schmidt, U., Weigert, M., Broaddus, C., and Myers, G. (2018). Cell Detection with Star-Convex Polygons. In Medical Image Computing and Computer Assisted Intervention – MICCAI 2018, A.F. Frangi, J.A. Schnabel, C. Davatzikos, C. Alberola-López, and G. Fichtinger, eds. (Springer International Publishing), pp. 265–273. https://doi.org/10.1007/978-3-030-00934-2_30.

41. Schürch, C.M., Bhate, S.S., Barlow, G.L., Phillips, D.J., Noti, L., Zlobec, I., Chu, P., Black, S., Demeter, J., McIlwain, D.R., et al. (2020). Coordinated Cellular Neighborhoods Orchestrate Antitumoral Immunity at the Colorectal Cancer Invasive Front. Cell *182*, 1341–1359.e19. https://doi.org/10.1016/j.cell.2020.07.005.

42. Hu, Y., Rong, J., Xu, Y., Xie, R., Peng, J., Gao, L., Tan, K., Hu, Y., Rong, J., and Xu, Y. (2024). Unsupervised and supervised discovery of tissue cellular neighborhoods from cell phenotypes. Nat. Methods *21*, 267–278. https://doi.org/10.1038/s41592-023-02124-2.

43. Varrone, M., Tavernari, D., Santamaria-Martínez, A., Walsh, L.A., and Ciriello, G. (2024). CellCharter reveals spatial cell niches associated with tissue remodeling and cell plasticity. Nat. Genet. *56*, 74–84. https://doi.org/10.1038/s41588-023-01588-4.

44. Birk, S., Bonafonte-Pardàs, I., Feriz, A.M., Boxall, A., Agirre, E., Memi, F., Maguza, A., Yadav, A., Armingol, E., Fan, R., et al. (2025). Quantitative characterization of cell niches in spatially resolved omics data. Nat. Genet. *57*, 897–909. https://doi.org/10.1038/s41588-025-02120-6.

45. Hu, J., Sánchez-Rivera, F.J., Wang, Z., Johnson, G.N., Ho, Y.J., Ganesh, K., Umeda, S., Gan, S., Mujal, A.M., Delconte, R.B., et al. (2023). STING inhibits the reactivation of dormant metastasis in lung adenocarcinoma. Nature *616*, 806–813. https://doi.org/10.1038/s41586-023-05880-5.

46. Zhang, B., Ren, Z., Zheng, H., Lin, M., Chen, G., Luo, O.J., and Zhu, G. (2023). CRISPR activation screening in a mouse model for drivers of hepatocellular carcinoma growth and metastasis. iScience *26*, 106099. https://doi.org/10.1016/j.isci.2023.106099.

47. Ester, M., Kriegel, H.-P., Sander, J., and Xu, X. (1996). A density-based algorithm for discovering clusters in large spatial databases with noise. KDD'96: Proceedings of the Second International Conference on Knowledge Discovery and Data Mining *34*, 226–231.

48. Van Seventer, G.A., Shimizu, Y., Horgan, K.J., and Shaw, S. (1990). The LFA-1 ligand ICAM-1 provides an important costimulatory signal for T cell receptor-mediated activation of resting T cells. J. Immunol. *144*, 4579–4586. https://doi.org/10.4049/jimmunol.144.12.4579.

49. Kohlmeier, J.E., Rumsey, L.M., Chan, M.A., and Benedict, S.H. (2003). The outcome of T-cell costimulation through intercellular adhesion molecule-1 differs from costimulation through leucocyte function-associated antigen-1. Immunology *108*, 152–157. https://doi.org/10.1046/j.1365-2567.2003.01578.x.

50. Ma, V.P.Y., Hu, Y., Kellner, A.V., Brockman, J.M., Velusamy, A., Blanchard, A.T., Evavold, B.D., Alon, R., and Salaita, K. (2022). The magnitude of LFA-1/ICAM-1 forces fine-tune TCR-triggered T cell activation. Sci. Adv. *8*, eabg4485. https://doi.org/10.1126/sciadv.abg4485.

51. Lacouture, C., Chaves, B., Guipouy, D., Houmadi, R., Duplan-Eche, V., Allart, S., Destainville, N., Dupré, L., Lacouture, C., and Chaves, B. (2024). LFA-1 nanoclusters integrate TCR stimulation strength to tune T-cell cytotoxic activity. Nat. Commun. *15*, 407. https://doi.org/10.1038/s41467-024-44688-3.

52. Zhou, X., Xu, T., Li, C., He, Y., Hu, Y., Gong, H., Li, J., Jiang, H., Wen, L., Fu, Y., et al. (2025). Potentiating anti-tumor immunity by re-engaging immune synapse molecules. Cell Rep. Med. *6*, 101975. https://doi.org/10.1016/j.xcrm.2025.101975.

53. Chapoval, A.I., Ni, J., Lau, J.S., Wilcox, R.A., Flies, D.B., Liu, D., Dong, H., Sica, G.L., Zhu, G., Tamada, K., and Chen, L. (2001). B7-H3: a costimulatory molecule for T cell activation and IFN-gamma production. Nat. Immunol. *2*, 269–274. https://doi.org/10.1038/85339.

54. Chen, M.-M., Gao, Q., Ning, H., Chen, K., Gao, Y., Yu, M., Liu, C.-Q., Zhou, W., Pan, J., Wei, L., et al. (2025). Integrated single-cell and spatial transcriptomics uncover distinct cellular subtypes involved in neural invasion in pancreatic cancer. Cancer Cell *43*, 1656–1676.e10. https://doi.org/10.1016/j.ccell.2025.06.020.

55. Kaczanowska, S., Beury, D.W., Gopalan, V., Tycko, A.K., Qin, H., Clements, M.E., Drake, J., Nwanze, C., Murgai, M., Rae, Z., et al. (2021). Genetically engineered myeloid cells rebalance the core immune suppression program in metastasis. Cell *184*, 2033–2052.e21. https://doi.org/10.1016/j.cell.2021.02.048.

56. Wang, S., Wang, J., Chen, Z., Luo, J., Guo, W., Sun, L., Lin, L., Wang, S., Wang, J., and Chen, Z. (2024). Targeting M2-like tumor-associated macrophages is a potential therapeutic approach to overcome antitumor drug resistance. npj Precis. Oncol. *8*, 31. https://doi.org/10.1038/s41698-024-00522-z.

57. Giles, J.R., Globig, A.M., Kaech, S.M., and Wherry, E.J. (2023). CD8+ T cells in the cancer-immunity cycle. Immunity *56*, 2231–2253. https://doi.org/10.1016/j.immuni.2023.09.005.

58. Hu, Z., Yuan, J., Long, M., Jiang, J., Zhang, Y., Zhang, T., Xu, M., Fan, Y., Tanyi, J.L., Montone, K.T., et al. (2021). The Cancer Surfaceome Atlas integrates genomic, functional and drug response data to identify actionable targets. Nat. Cancer *2*, 1406–1422. https://doi.org/10.1038/s43018-021-00282-w.

59. Karlsson, M., Zhang, C., Méar, L., Zhong, W., Digre, A., Katona, B., Sjöstedt, E., Butler, L., Odeberg, J., Dusart, P., et al. (2021). A single–cell type transcriptomics map of human tissues. Sci. Adv. *7*, eabh2169. https://doi.org/10.1126/sciadv.abh2169.

60. Lambert, S.A., Jolma, A., Campitelli, L.F., Das, P.K., Yin, Y., Albu, M., Chen, X., Taipale, J., Hughes, T.R., and Weirauch, M.T. (2018). The Human Transcription Factors. Cell *172*, 650–665. https://doi.org/10.1016/j.cell.2018.01.029.

61. Uhlen, M., Karlsson, M.J., Zhong, W., Tebani, A., Pou, C., Mikes, J., Lakshmikanth, T., Forsström, B., Edfors, F., Odeberg, J., et al. (2019). A genome-wide transcriptomic analysis of protein-coding genes in human blood cells. Science *366*, eaax9198. https://doi.org/10.1126/science.aax9198.

62. Zeng, J., Zhang, Y., Shang, Y., Mai, J., Shi, S., Lu, M., Bu, C., Zhang, Z., Zhang, Z., Li, Y., et al. (2022). CancerSCEM: a database of single-cell expression map across various human cancers. Nucleic Acids Res. *50*, D1147–D1155. https://doi.org/10.1093/nar/gkab905.

63. Shi, M., Méar, L., Karlsson, M., Álvez, M.B., Digre, A., Schutten, R., Katona, B., Vuu, J., Lindström, E., Hikmet, F., et al. (2025). A resource for whole-body gene expression map of human tissues based on integration of single cell and bulk transcriptomics. Genome Biol. *26*, 152. https://doi.org/10.1186/s13059-025-03616-4.

64. Li, W., Xu, H., Xiao, T., Cong, L., Love, M.I., Zhang, F., Irizarry, R.A., Liu, J. S., Brown, M., and Liu, X.S. (2014). MAGeCK enables robust identification of essential genes from genome-scale CRISPR/Cas9 knockout screens. Genome Biol. *15*, 554. https://doi.org/10.1186/s13059-014-0554-4.

65. Wei, J., Long, L., Zheng, W., Dhungana, Y., Lim, S.A., Guy, C., Wang, Y., Wang, Y.D., Qian, C., Xu, B., et al. (2019). Targeting REGNASE-1 programs long-lived effector T cells for cancer therapy. Nature *576*, 471–476. https://doi.org/10.1038/s41586-019-1821-z.

66. Singer, M., Wang, C., Cong, L., Marjanovic, N.D., Kowalczyk, M.S., Zhang, H., Nyman, J., Sakuishi, K., Kurtulus, S., Gennert, D., et al. (2016). A Distinct Gene Module for Dysfunction Uncoupled from

Activation in Tumor-Infiltrating T Cells. Cell *166*, 1500–1511.e9. https://doi.org/10.1016/j.cell.2016.08.052.

67. Cao, Y., Trillo-Tinoco, J., Sierra, R.A., Anadon, C., Dai, W., Mohamed, E., Cen, L., Costich, T.L., Magliocco, A., Marchion, D., et al. (2019). ER stress-induced mediator C/EBP homologous protein thwarts effector T cell activity in tumors through T-bet repression. Nat. Commun. *10*, 1280. https://doi.org/10.1038/s41467-019-09263-1.

68. Tomihari, M., Chung, J.S., Akiyoshi, H., Cruz, P.D., Jr., and Ariizumi, K. (2010). DC-HIL/glycoprotein Nmb promotes growth of melanoma in mice by inhibiting the activation of tumor-reactive T cells. Cancer Res. *70*, 5778–5787. https://doi.org/10.1158/0008-5472.CAN-09-2538.

69. Zhang, J., Li, J., Hou, Y., Lin, Y., Zhao, H., Shi, Y., Chen, K., Nian, C., Tang, J., Pan, L., et al. (2024). Osr2 functions as a biomechanical checkpoint to aggravate CD8+ T cell exhaustion in tumor. Cell *187*, 3409–3426.e24. https://doi.org/10.1016/j.cell.2024.04.023.

70. Huai, W., Yang, K., Xing, C., Song, K., Lyu, H., Williams, N.S., Wu, J., and Yan, N. (2025). OAS cross-activates RNase L intercellularly through cell-to-cell transfer of 2–5A to spread innate immunity. Immunity *58*, 797–810.e6. https://doi.org/10.1016/j.immuni.2025.01.016.

71. Fang, F., Cao, W., Zhu, W., Lam, N., Li, L., Gaddam, S., Wang, Y., Kim, C., Lambert, S., Zhang, H., et al. (2021). The cell-surface 5'-nucleotidase CD73 defines a functional T memory cell subset that declines with age. Cell Rep. *37*, 109981. https://doi.org/10.1016/j.celrep.2021.109981.

72. Yenyuwadee, S., Sanchez-Trincado Lopez, J.L., Shah, R., Rosato, P.C., and Boussiotis, V.A. (2022). The evolving role of tissue-resident memory T cells in infections and cancer. Sci. Adv. *8*, eabo5871. https://doi.org/10.1126/sciadv.abo5871.

73. Crowl, J.T., Heeg, M., Ferry, A., Milner, J.J., Omilusik, K.D., Toma, C., He, Z., Chang, J.T., and Goldrath, A.W. (2022). Tissue-resident memory CD8+ T cells possess unique transcriptional, epigenetic and functional adaptations to different tissue environments. Nat. Immunol. *23*, 1121–1131. https://doi.org/10.1038/s41590-022-01229-8.

74. Krishna, S., Lowery, F.J., Copeland, A.R., Bahadiroglu, E., Mukherjee, R., Jia, L., Anibal, J.T., Sachs, A., Adebola, S.O., Gurusamy, D., et al. (2020). Stem-like CD8 T cells mediate response of adoptive cell immunotherapy against human cancer. Science *370*, 1328–1334. https://doi.org/10.1126/science.abb9847.

75. Buck, M.D., O'Sullivan, D., Klein Geltink, R.I., Curtis, J.D., Chang, C.H., Sanin, D.E., Qiu, J., Kretz, O., Braas, D., van der Windt, G.J.W., et al. (2016). Mitochondrial Dynamics Controls T Cell Fate through Metabolic Programming. Cell *166*, 63–76. https://doi.org/10.1016/j.cell.2016.05.035.

76. Gattinoni, L., Speiser, D.E., Lichterfeld, M., Bonini, C., Gattinoni, L., Speiser, D.E., Lichterfeld, M., and Bonini, C. (2017). T memory stem cells in health and disease. Nat. Med. *23*, 18–27. https://doi.org/10.1038/nm.4241.

77. Yu, Y.R., Imrichova, H., Wang, H., Chao, T., Xiao, Z., Gao, M., Rincon-Restrepo, M., Franco, F., Genolet, R., Cheng, W.C., et al. (2020). Disturbed mitochondrial dynamics in CD8+ TILs reinforce T cell exhaustion. Nat. Immunol. *21*, 1540–1551. https://doi.org/10.1038/s41590-020-0793-3.

78. Funauchi, M., Serada, S., Hiramatsu, K., Funajima, E., Kanda, M., Nagase, Y., Nakagawa, S., Ohkawara, T., Fujimoto, M., Suzuki, Y., et al. (2024). Tumor cell-expressed lipolysis-stimulated lipoprotein receptor negatively regulates T-cell function. Int. J. Cancer *154*, 425–433. https://doi.org/10.1002/ijc.34738.

79. Lu, J., Chatterjee, M., Schmid, H., Beck, S., and Gawaz, M. (2016). CXCL14 as an emerging immune and inflammatory modulator. J. Inflamm. (Lond) *13*, 1. https://doi.org/10.1186/s12950-015-0109-9.

80. Klement, J.D., Paschall, A.V., Redd, P.S., Ibrahim, M.L., Lu, C., Yang, D., Celis, E., Abrams, S.I., Ozato, K., and Liu, K. (2018). An osteopontin/CD44 immune checkpoint controls CD8+ T cell activation and tumor immune evasion. J. Clin. Investig. *128*, 5549–5560. https://doi.org/10.1172/JCI123360.

81. Yan, Y., Sun, D., Hu, J., Chen, Y., Sun, L., Yu, H., Xiong, Y., Huang, Z., Xia, H., Zhu, X., et al. (2025). Multi-omic profiling highlights factors associated with resistance to immuno-chemotherapy in non-small-cell lung cancer. Nat. Genet. *57*, 126–139. https://doi.org/10.1038/s41588-024-01998-y.

82. Waibl Polania, J., Hoyt-Miggelbrink, A., Tomaszewski, W.H., Wachsmuth, L.P., Lorrey, S.J., Wilkinson, D.S., Lerner, E., Woroniecka, K., Finlay, J.B., Ayasoufi, K., and Fecci, P.E. (2025). Antigen presentation by tumor-associated macrophages drives T cells from a progenitor exhaustion state to terminal exhaustion. Immunity *58*, 232–246.e6. https://doi.org/10.1016/j.immuni.2024.11.026.

83. Elewaut, A., Estivill, G., Bayerl, F., Castillon, L., Novatchkova, M., Pottendorfer, E., Hoffmann-Haas, L., Schönlein, M., Nguyen, T.V., Lauss, M., et al. (2025). Cancer cells impair monocyte-mediated T cell stimulation to evade immunity. Nature *637*, 716–725. https://doi.org/10.1038/s41586-024-08257-4.

84. Cheng, M., Liang, G., Yin, Z., Lin, X., Sun, Q., and Liu, Y. (2023). Immunosuppressive role of SPP1-CD44 in the tumor microenvironment of intrahepatic cholangiocarcinoma assessed by single-cell RNA sequencing. J. Cancer Res. Clin. Oncol. *149*, 5497–5512. https://doi.org/10.1007/s00432-022-04498-w.

85. Bill, R., Wirapati, P., Messemaker, M., Roh, W., Zitti, B., Duval, F., Kiss, M., Park, J.C., Saal, T.M., Hoelzl, J., et al. (2023). CXCL9:SPP1 macrophage polarity identifies a network of cellular programs that control human cancers. Science *381*, 515–524. https://doi.org/10.1126/science.ade2292.

86. He, H., Chen, S., Fan, Z., Dong, Y., Wang, Y., Li, S., Sun, X., Song, Y., Yang, J., Cao, Q., et al. (2023). Multi-dimensional single-cell characterization revealed suppressive immune microenvironment in AFP-positive hepatocellular carcinoma. Cell Discov. *9*, 60. https://doi.org/10.1038/s41421-023-00563-x.

87. Cheng, J.-N., Jin, Z., Su, C., Jiang, T., Zheng, X., Guo, J., Li, X., Chu, H., Jia, J., Zhou, Q., et al. (2025). Bone metastases diminish extraosseous response to checkpoint blockade immunotherapy through osteopontin-producing osteoclasts. Cancer Cell *43*, 1093–1107.e9. https://doi.org/10.1016/j.ccell.2025.03.036.

88. Vasilevska, J., Cheng, P.F., Lehmann, J., Ramelyte, E., Gomez, J.M., Dimitriou, F., Sella, F., TuPro, C., Ferretti, D., Salas-Bastos, A., et al. (2024). Monitoring melanoma patients on treatment reveals a distinct macrophage population driving targeted therapy resistance. Cell. Reprod. Med. *5*, 101611.

89. Weber, G.F., Ashkar, S., Glimcher, M.J., and Cantor, H. (1996). Receptor-ligand interaction between CD44 and osteopontin (Eta-1). Science *271*, 509–512. https://doi.org/10.1126/science.271.5248.509.

90. Hoeft, K., Schaefer, G.J.L., Kim, H., Schumacher, D., Bleckwehl, T., Long, Q., Klinkhammer, B.M., Peisker, F., Koch, L., Nagai, J., et al. (2023). Platelet-instructed SPP1+ macrophages drive myofibroblast activation in fibrosis in a CXCL4-dependent manner. Cell Rep. *42*, 112131. https://doi.org/10.1016/j.celrep.2023.112131.

91. Lin, Y.H., and Yang-Yen, H.F. (2001). The osteopontin-CD44 survival signal involves activation of the phosphatidylinositol 3-kinase/Akt signaling pathway. J. Biol. Chem. *276*, 46024–46030. https://doi.org/10.1074/jbc.M105132200.

92. Solier, S., Müller, S., Cañeque, T., Versini, A., Mansart, A., Sindikubwabo, F., Baron, L., Emam, L., Gestraud, P., Pantoş, G.D., et al. (2023). A druggable copper-signalling pathway that drives inflammation. Nature *617*, 386–394. https://doi.org/10.1038/s41586-023-06017-4.

93. Cañeque, T., Baron, L., Müller, S., Carmona, A., Colombeau, L., Versini, A., Solier, S., Gaillet, C., Sindikubwabo, F., Sampaio, J.L., et al. (2025). Activation of lysosomal iron triggers ferroptosis in cancer. Nature *642*, 492–500. https://doi.org/10.1038/s41586-025-08974-4.

94. Tang, D., Chen, X., Kang, R., Kroemer, G., Tang, D., Chen, X., Kang, R., and Kroemer, G. (2020). Ferroptosis: molecular mechanisms and health implications. Cell Res. *31*, 107–125. https://doi.org/10.1038/s41422-020-00441-1.

95. Voss, K., Sewell, A.E., Krystofiak, E.S., Gibson-Corley, K.N., Young, A.C., Basham, J.H., Sugiura, A., Arner, E.N., Beavers, W.N., Kunkle, D.E., et al. (2023). Elevated transferrin receptor impairs T cell metabolism and

function in systemic lupus erythematosus. Sci. Immunol. *8*, eabq0178. https://doi.org/10.1126/sciimmunol.abq0178.

96. Matsushita, M., Freigang, S., Schneider, C., Conrad, M., Bornkamm, G. W., and Kopf, M. (2015). T cell lipid peroxidation induces ferroptosis and prevents immunity to infection. J. Exp. Med. *212*, 555–568. https://doi.org/10.1084/jem.20140857.

97. Dixon, S.J., and Stockwell, B.R. (2014). The role of iron and reactive oxygen species in cell death. Nat. Chem. Biol. *10*, 9–17. https://doi.org/10.1038/nchembio.1416.

98. Dixon, S.J., Lemberg, K.M., Lamprecht, M.R., Skouta, R., Zaitsev, E.M., Gleason, C.E., Patel, D.N., Bauer, A.J., Cantley, A.M., Yang, W.S., et al. (2012). Ferroptosis: an iron-dependent form of nonapoptotic cell death. Cell *149*, 1060–1072. https://doi.org/10.1016/j.cell.2012.03.042.

99. Weinberg, S.E., and Chandel, N.S. (2025). Mitochondria reactive oxygen species signaling in immune responses. Immunity *58*, 1904–1921. https://doi.org/10.1016/j.immuni.2025.07.012.

100. Chang, C.-H., Curtis, J.D., Maggi, L.B., Faubert, B., Villarino, A.V., O'Sullivan, D., Huang, S.C.-C., van der Windt, G.J.W., Blagih, J., Qiu, J., et al. (2013). Posttranscriptional Control of T Cell Effector Function by Aerobic Glycolysis. Cell *153*, 1239–1251. https://doi.org/10.1016/j.cell.2013.05.016.

101. Stockwell, B.R. (2022). Ferroptosis turns 10: Emerging mechanisms, physiological functions, and therapeutic applications. Cell *185*, 2401–2421. https://doi.org/10.1016/j.cell.2022.06.003.

102. Xie, B., Guo, Y., Xie, B., and Guo, Y. (2021). Molecular mechanism of cell ferroptosis and research progress in regulation of ferroptosis by noncoding RNAs in tumor cells. Cell Death Discov. *7*, 101. https://doi.org/10.1038/s41420-021-00483-3.

103. Gomez-Roca, C., Cassier, P., Zamarin, D., Machiels, J.P., Perez Gracia, J.L., Stephen Hodi, F., Taus, A., Martinez Garcia, M., Boni, V., Eder, J.P., et al. (2022). Anti-CSF-1R emactuzumab in combination with anti-PD-L1 atezolizumab in advanced solid tumor patients naive or experienced for immune checkpoint blockade. J. Immunother. Cancer *10*, e004076. https://doi.org/10.1136/jitc-2021-004076.

104. Lu, Y., Luo, C., Huang, L., Wu, G., Zhong, L., Chu, J., Wang, F., Zeng, Z., and Pan, D. (2025). Functional genetic screens reveal key pathways instructing the molecular phenotypes of tumor-associated macrophages. Cancer Immunol. Res. *13*, 2054–2074. https://doi.org/10.1158/2326-6066.CIR-25-0488.

105. Andreatta, M., Corria-Osorio, J., Müller, S., Cubas, R., Coukos, G., Carmona, S.J., Andreatta, M., Corria-Osorio, J., Müller, S., and Cubas, R. (2021). Interpretation of T cell states from single-cell transcriptomics data using reference atlases. Nat. Commun. *12*, 2965. https://doi.org/10.1038/s41467-021-23324-4.

106. Chu, Y., Dai, E., Li, Y., Han, G., Pei, G., Ingram, D.R., Thakkar, K., Qin, J.-J., Dang, M., Le, X., et al. (2023). Pan-cancer T cell atlas links a cellular stress response state to immunotherapy resistance. Nat. Med. *29*, 1550–1562. https://doi.org/10.1038/s41591-023-02371-y.

107. Di Pilato, M., Kfuri-Rubens, R., Pruessmann, J.N., Ozga, A.J., Messemaker, M., Cadilha, B.L., Sivakumar, R., Cianciaruso, C., Warner, R.D., Marangoni, F., et al. (2021). CXCR6 positions cytotoxic T cells to receive critical survival signals in the tumor microenvironment. Cell *184*, 4512–4530.e22. https://doi.org/10.1016/j.cell.2021.07.015.

108. Aibar, S., González-Blas, C.B., Moerman, T., Huynh-Thu, V.A., Imrichova, H., Hulselmans, G., Rambow, F., Marine, J.C., Geurts, P., Aerts, J., et al. (2017). SCENIC: single-cell regulatory network inference and clustering. Nat. Methods *14*, 1083–1086. https://doi.org/10.1038/nmeth.4463.

109. Park, S.L., and Mackay, L.K. (2019). Bhlhe40 Keeps Resident T Cells Too Fit to Quit. Immunity *51*, 418–420. https://doi.org/10.1016/j.immuni.2019.08.016.

110. Li, C., Zhu, B., Son, Y.M., Wang, Z., Jiang, L., Xiang, M., Ye, Z., Beckermann, K.E., Wu, Y., Jenkins, J.W., et al. (2019). The Transcription Factor Bhlhe40 Programs Mitochondrial Regulation of Resident CD8+ T Cell Fitness and Functionality. Immunity *51*, 491–507.e7. https://doi.org/10.1016/j.immuni.2019.08.013.

111. Steele, M.M., Jaiswal, A., Delclaux, I., Dryg, I.D., Murugan, D., Femel, J., Son, S., Du Bois, H., Hill, C., Leachman, S.A., et al. (2023). T cell egress via lymphatic vessels is tuned by antigen encounter and limits tumor control. Nat. Immunol. *24*, 664–675. https://doi.org/10.1038/s41590-023-01443-y.

112. Li, E., Cheung, H.C.Z., and Ma, S. (2024). CTHRC1+ fibroblasts and SPP1+ macrophages synergistically contribute to pro-tumorigenic tumor microenvironment in pancreatic ductal adenocarcinoma. Sci. Rep. *14*, 17412. https://doi.org/10.1038/s41598-024-68109-z.

113. Nallasamy, P., Nimmakayala, R.K., Karmakar, S., Leon, F., Seshacharyulu, P., Lakshmanan, I., Rachagani, S., Mallya, K., Zhang, C., Ly, Q.P., et al. (2021). Pancreatic Tumor Microenvironment Factor Promotes Cancer Stemness via SPP1-CD44 Axis. Gastroenterology *161*, 1998–2013.e7. https://doi.org/10.1053/j.gastro.2021.08.023.

114. Trehan, R., Huang, P., Zhu, X.B., Wang, X., Soliman, M., Strepay, D., Nur, A., Kedei, N., Arhin, M., Ghabra, S., et al. (2025). SPP1 + macrophages cause exhaustion of tumor-specific T cells in liver metastases. Nat. Commun. *16*, 4242. https://doi.org/10.1038/s41467-025-59529-0.

115. Meiser, P., Knolle, M.A., Hirschberger, A., de Almeida, G.P., Bayerl, F., Lacher, S., Pedde, A.M., Flommersfeld, S., Hönninger, J., Stark, L., et al. (2023). A distinct stimulatory cDC1 subpopulation amplifies CD8+ T cell responses in tumors for protective anti-cancer immunity. Cancer Cell *41*, 1498–1515.e10. https://doi.org/10.1016/j.ccell.2023.06.008.

116. Lin, C.P., Levy, P.L., Alflen, A., Apriamashvili, G., Ligtenberg, M.A., Vredevoogd, D.W., Bleijerveld, O.B., Alkan, F., Malka, Y., Hoekman, L., et al. (2024). Multimodal stimulation screens reveal unique and shared genes limiting T cell fitness. Cancer Cell *42*, 623–645.e10. https://doi.org/10.1016/j.ccell.2024.02.016.

117. Wu, J.E., Manne, S., Ngiow, S.F., Baxter, A.E., Huang, H., Freilich, E., Clark, M.L., Lee, J.H., Chen, Z., Khan, O., et al. (2023). In vitro modeling of CD8(+) T cell exhaustion enables CRISPR screening to reveal a role for BHLHE40. Sci. Immunol. *8*, eade3369. https://doi.org/10.1126/sciimmunol.ade3369.

118. McDermott, D.F., Huseni, M.A., Atkins, M.B., Motzer, R.J., Rini, B.I., Escudier, B., Fong, L., Joseph, R.W., Pal, S.K., Reeves, J.A., et al. (2018). Clinical activity and molecular correlates of response to atezolizumab alone or in combination with bevacizumab versus sunitinib in renal cell carcinoma. Nat. Med. *24*, 749–757. https://doi.org/10.1038/s41591-018-0053-3.

119. Liu, D., Schilling, B., Liu, D., Sucker, A., Livingstone, E., Jerby-Arnon, L., Zimmer, L., Gutzmer, R., Satzger, I., Loquai, C., et al. (2019). Integrative molecular and clinical modeling of clinical outcomes to PD1 blockade in patients with metastatic melanoma. Nat. Med. *25*, 1916–1927. https://doi.org/10.1038/s41591-019-0654-5.

120. Wolf, F.A., Angerer, P., Theis, F.J., Wolf, F.A., Angerer, P., and Theis, F.J. (2018). SCANPY: large-scale single-cell gene expression data analysis. Genome Biol. *19*, 15. https://doi.org/10.1186/s13059-017-1382-0.

121. He, P., Williams, B.A., Trout, D., Marinov, G.K., Amrhein, H., Berghella, L., Goh, S.-T., Plajzer-Frick, I., Afzal, V., Pennacchio, L.A., et al. (2020). The changing mouse embryo transcriptome at whole tissue and single-cell resolution. Nature *583*, 760–767. https://doi.org/10.1038/s41586-020-2536-x.

122. Zeng, Z., Li, Y., Li, Y., and Luo, Y. (2022). Statistical and machine learning methods for spatially resolved transcriptomics data analysis. Genome Biol. *23*, 83. https://doi.org/10.1186/s13059-022-02653-7.

123. Kullback, S., and Leibler, R.A. (1951). On Information and Sufficiency. Ann. Math. Statist. *22*, 79–86. https://doi.org/10.1214/aoms/1177729694.

124. Aitchison, J. (1982). The Statistical-Analysis of Compositional Data. J. R. Stat. Soc. B *44*, 139–160. https://doi.org/10.1111/j.2517-6161.1982.tb01195.x.

125. Fisher, R.A. (1935). The Design of Experiments (Oliver & Boyd).

126. Benjamini, Y., and Hochberg, Y. (1995). Controlling the False Discovery Rate – a Practical and Powerful Approach to Multiple Testing. J. R. Stat. Soc. B *57*, 289–300. https://doi.org/10.1111/j.2517-6161.1995.tb02031.x.

127. Daunou, P.C.F. (1803). Mémoire sur les Élections au Scrutin (Baudouin).

128. Ramdas, A., Trillos, N.G., and Cuturi, M. (2017). On Wasserstein Two-Sample Testing and Related Families of Nonparametric Tests. Entropy *19*, 47. https://doi.org/10.3390/e19020047.

129. Rosenblatt, M. (1956). Remarks on Some Nonparametric Estimates of a Density-Function. Ann. Math. Statist. *27*, 832–837. https://doi.org/10.1214/aoms/1177728190.

130. Silverman, B. (1986). Density estimation for statistics and data analysis (Monographs on Statistics and Applied Probability).

131. Hershey, J.R., and Olsen, P.A. (2007). Approximating the Kullback Leibler Divergence between Gaussian Mixture Models. 2007 IEEE International Conference on Acoustics, Speech and Signal Processing - ICASSP '07. IV-317–IV-320. https://doi.org/10.1109/ICASSP.2007.366913.

132. Peidli, S., Green, T.D., Shen, C., Gross, T., Min, J., Garda, S., Yuan, B., Schumacher, L.J., Taylor-King, J.P., Marks, D.S., et al. (2024). scPerturb: harmonized single-cell perturbation data. Nat. Methods *21*, 531–540. https://doi.org/10.1038/s41592-023-02144-y.

133. Kolmogorov, A., and L.. (1933). Sulla determinazione empirica di una legge di distribuzione. G. Ist. Ital. Attuari *4*, 83–91.

134. Syrjala, S.E. (1996). A statistical test for a difference between the spatial distributions of two populations. Ecology *77*, 75–80. https://doi.org/10.2307/2265656.

135. Gong, D., Arbesfeld-Qiu, J.M., Perrault, E., Bae, J.W., and Hwang, W.L. (2024). Spatial oncology: Translating contextual biology to the clinic. Cancer Cell *42*, 1653–1675. https://doi.org/10.1016/j.ccell.2024.09.001.

136. Cui, A., Huang, T., Li, S., Ma, A., Pérez, J.L., Sander, C., Keskin, D.B., Wu, C.J., Fraenkel, E., and Hacohen, N. (2024). Dictionary of immune responses to cytokines at single-cell resolution. Nature *625*, 377–384. https://doi.org/10.1038/s41586-023-06816-9.

137. Schenkel, J.M., and Pauken, K.E. (2023). Localization, tissue biology and T cell state — implications for cancer immunotherapy. Nat. Rev. Immunol. *23*, 807–823. https://doi.org/10.1038/s41577-023-00884-8.

138. Borrelli, C., Roberts, M., Eletto, D., Hussherr, M.D., Fazilaty, H., Valenta, T., Lafzi, A., Kretz, J.A., Guido Vinzoni, E., Karakatsani, A., et al. (2024). In vivo interaction screening reveals liver-derived constraints to metastasis. Nature *632*, 411–418. https://doi.org/10.1038/s41586-024-07715-3.

139. He, Z., Maynard, A., Jain, A., Gerber, T., Petri, R., Lin, H.C., Santel, M., Ly, K., Dupré, J.S., Sidow, L., et al. (2022). Lineage recording in human cerebral organoids. Nat. Methods *19*, 90–99. https://doi.org/10.1038/s41592-021-01344-8.

140. Lam, S.K., Pitrou, A., and Seibert, S. (2015). Numba: a LLVM-based Python JIT compiler. In Proceedings of the Second Workshop on the LLVM Compiler Infrastructure in HPC (Association for Computing Machinery), pp. 1–6. https://doi.org/10.1145/2833157.2833162.

141. Anderson, M.J. (2001). A new method for non-parametric multivariate analysis of variance. Austral Ecol. *26*, 32–46.

142. Megas, S., Chen, D.G., Polanski, K., Asadollahzadeh, H., Eliasof, M., Schönlieb, C.-B., and Teichmann, S.A. (2026). Celcomen: spatial causal disentanglement for single-cell and tissue perturbation modeling. Published online March 18, 2026. Nat. Commun. https://doi.org/10.1038/s41467-026-69856-5.

143. Wang, X., Allen, W.E., Wright, M.A., Sylwestrak, E.L., Samusik, N., Vesuna, S., Evans, K., Liu, C., Ramakrishnan, C., Liu, J., et al. (2018). Three-dimensional intact-tissue sequencing of single-cell transcriptional states. Science *361*, eaat5691. https://doi.org/10.1126/science.aat5691.

144. Kanatani, S., Kreutzmann, J.C., Li, Y., West, Z., Larsen, L.L., Nikou, D.V., Eidhof, I., Walton, A., Zhang, S., Rodríguez-Kirby, L.R., et al. (2024). Whole-brain spatial transcriptional analysis at cellular resolution. Science *386*, 907–915. https://doi.org/10.1126/science.adn9947.

145. Schott, M., León-Periñán, D., Splendiani, E., Strenger, L., Licha, J.R., Pentimalli, T.M., Schallenberg, S., Alles, J., Samut Tagliaferro, S., Boltengagen, A., et al. (2024). Open-ST: High-resolution spatial transcriptomics in 3D. Cell *187*, 3953–3972.e26. https://doi.org/10.1016/j.cell.2024.05.055.

146. Yang, L., Wang, J., Altreuter, J., Jhaveri, A., Wong, C.J., Song, L., Fu, J., Taing, L., Bodapati, S., Sahu, A., et al. (2023). Tutorial: integrative computational analysis of bulk RNA-sequencing data to characterize tumor immunity using RIMA. Nat. Protoc. *18*, 2404–2414. https://doi.org/10.1038/s41596-023-00841-8.

147. Birsoy, K., Wang, T., Chen, W.W., Freinkman, E., Abu-Remaileh, M., and Sabatini, D.M. (2015). An Essential Role of the Mitochondrial Electron Transport Chain in Cell Proliferation Is to Enable Aspartate Synthesis. Cell *162*, 540–551. https://doi.org/10.1016/j.cell.2015.07.016.

148. Doench, J.G., Fusi, N., Sullender, M., Hegde, M., Vaimberg, E.W., Donovan, K.F., Smith, I., Tothova, Z., Wilen, C., Orchard, R., et al. (2016). Optimized sgRNA design to maximize activity and minimize off-target effects of CRISPR-Cas9. Nat. Biotechnol. *34*, 184–191. https://doi.org/10.1038/nbt.3437.

149. Sade-Feldman, M., Yizhak, K., Bjorgaard, S.L., Ray, J.P., de Boer, C.G.D., Jenkins, R.W., Lieb, D.J., Chen, J.H., Frederick, D.T., Barzily-Rokni, M., et al. (2018). Defining T Cell States Associated with Response to Checkpoint Immunotherapy in Melanoma. Cell *175*, 998–1013.e20. https://doi.org/10.1016/j.cell.2018.10.038.

150. Jerby-Arnon, L., Shah, P., Cuoco, M.S., Rodman, C., Su, M.-J., Melms, J.C., Leeson, R., Kanodia, A., Mei, S., Lin, J.-R., et al. (2018). A Cancer Cell Program Promotes T Cell Exclusion and Resistance to Checkpoint Blockade. Cell *175*, 984–997.e24. https://doi.org/10.1016/j.cell.2018.09.006.

151. Yost, K.E., Satpathy, A.T., Wells, D.K., Qi, Y., Wang, C., Kageyama, R., McNamara, K.L., Granja, J.M., Sarin, K.Y., Brown, R.A., et al. (2019). Clonal replacement of tumor-specific T cells following PD-1 blockade. Nat. Med. *25*, 1251–1259. https://doi.org/10.1038/s41591-019-0522-3.

152. Paulson, K.G., Voillet, V., McAfee, M.S., Hunter, D.S., Wagener, F.D., Perdicchio, M., Valente, W.J., Koelle, S.J., Church, C.D., Vandeven, N., et al. (2018). Acquired cancer resistance to combination immunotherapy from transcriptional loss of class I HLA. Nat. Commun. *9*, 3868. https://doi.org/10.1038/s41467-018-06300-3.

153. Van Allen, E.M.V., Miao, D., Schilling, B., Shukla, S.A., Blank, C., Zimmer, L., Sucker, A., Hillen, U., Foppen, M.H.G., Goldinger, S.M., et al. (2015). Genomic correlates of response to CTLA-4 blockade in metastatic melanoma. Science *350*, 207–211. https://doi.org/10.1126/science.aad0095.